6190–6207 *Nucleic Acids Research, 2023, Vol. 51, No. 12* *Published online 13 May 2023*
https://doi.org/10.1093/nar/gkad387

Epigenetic plasticity safeguards heterochromatin configuration in mammals

Kei Fukuda[1,14,*], Takeshi Shimi[2,3], Chikako Shimura[1], Takao Ono[4], Takehiro Suzuki[5], Kenta Onoue[6], Satoko Okayama[6], Hisashi Miura[7], Ichiro Hiratani[7], Kazuho Ikeda[8], Yasushi Okada[8,9,10,11], Naoshi Dohmae[5], Shigenobu Yonemura[6,12], Azusa Inoue[15,16], Hiroshi Kimura[2,3,13] and Yoichi Shinkai[1,*]

[1]Cellular Memory Laboratory, RIKEN Cluster for Pioneering Research, Wako 351-0198, Japan, [2]World Research Hub Initiative, Institute of Innovative Research, Tokyo Institute of Technology, Yokohama 226-8503, Japan, [3]Cell Biology Center, Institute of Innovative Research, Tokyo Institute of Technology, Yokohama 226-8503, Japan, [4]Chromosome Dynamics Laboratory, RIKEN Cluster for Pioneering Research, Wako 351-0198, Japan, [5]Biomolecular Characterization Unit, Technology Platform Division, RIKEN Center for Sustainable Resource Science, Wako 351-0198, Japan, [6]Laboratory for Ultrastructural Research, RIKEN Center for Biosystems Dynamics Research, Kobe 650-0047, Japan, [7]Laboratory for Developmental Epigenetics, RIKEN Center for Biosystems Dynamics Research, Kobe 650-0047, Japan, [8]Department of Cell Biology, Graduate School of Medicine, The University of Tokyo, Tokyo 113-0033, Japan, [9]Universal Biology Institute (UBI) and International Research Center for Neurointelligence (WPI-IRCN), The University of Tokyo, Tokyo 113-0033, Japan, [10]Laboratory for Cell Polarity Regulation, RIKEN Center for Biosystems Dynamics Research (BDR), Osaka 565-0874, Japan, [11]Department of Physics, Graduate School of Science, The University of Tokyo, Tokyo 113-0033, Japan, [12]Department of Cell Biology, Tokushima University Graduate School of Medicine, Tokushima 770-8503, Japan, [13]School of Life Science and Technology, Tokyo Institute of Technology, Yokohama 226-8501, Japan, [14]School of Biosciences, The University of Melbourne, Royal Parade, 3010 Parkville, Australia, [15]Laboratory for Epigenome Inheritance, RIKEN Center for Integrative Medical Sciences, Yokohama 230-0045, Japan and [16]Tokyo Metropolitan University, Hachioji 192-0397, Japan

Received October 03, 2022; Revised April 13, 2023; Editorial Decision April 25, 2023; Accepted May 02, 2023

ABSTRACT

Heterochromatin is a key architectural feature of eukaryotic chromosomes critical for cell type-specific gene expression and genome stability. In the mammalian nucleus, heterochromatin segregates from transcriptionally active genomic regions and exists in large, condensed, and inactive nuclear compartments. However, the mechanisms underlying the spatial organization of heterochromatin need to be better understood. Histone H3 lysine 9 trimethylation (H3K9me3) and lysine 27 trimethylation (H3K27me3) are two major epigenetic modifications that enrich constitutive and facultative heterochromatin, respectively. Mammals have at least five H3K9 methyltransferases (SUV39H1, SUV39H2, SETDB1, G9a and GLP) and two H3K27 methyltransferases (EZH1 and EZH2). In this study, we addressed the role of H3K9 and H3K27 methylation in heterochromatin organization using a combination of mutant cells for five H3K9 methyltransferases and an EZH1/2 dual inhibitor, DS3201. We showed that H3K27me3, which is normally segregated from H3K9me3, was redistributed to regions targeted by H3K9me3 after the loss of H3K9 methylation and that the loss of both H3K9 and H3K27 methylation resulted in impaired condensation and spatial organization of heterochromatin. Our data demonstrate that the H3K27me3 pathway safeguards heterochromatin organization after the loss of H3K9 methylation in mammalian cells.

*To whom correspondence should be addressed. Tel: +81 48 467 9370; Fax: +81 48 462 4670; Email: yshinkai@riken.jp
Correspondence may also be addressed to Kei Fukuda. Tel: +61 412 614 421; Email: kefukuda8@gmail.com

GRAPHICAL ABSTRACT

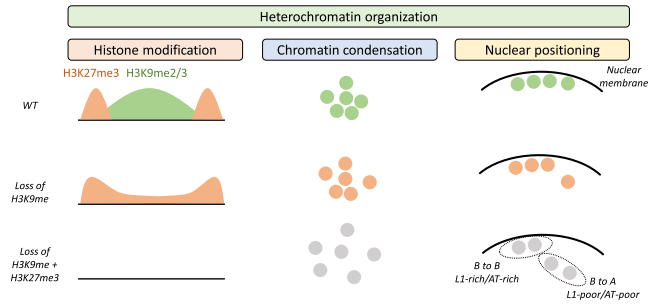

INTRODUCTION

The eukaryotic genome is divided into two domains: euchromatin and heterochromatin. Heterochromatin appears as an electron-dense structure in an electron microscopic image of the nucleus, which is distinct from the looser form of euchromatin and plays essential roles in genome stability, chromosome segregation, and silencing of cell type-specific gene expression (1). Heterochromatin is spatially segregated from euchromatin and is frequently found in the nuclear periphery. Recent developments in chromosome conformation capture techniques such as Hi-C have revealed that euchromatin and heterochromatin form active (A) and inactive (B) compartments, respectively (2). Although the A/B compartments correlate well with gene activation/repression, the molecular determinants of compartmental forces remain largely unknown. Furthermore, B compartments are associated with lamina-associated domains (LADs) (3–5), which interact with the nuclear lamina (NL) and late replicating regions (6). Although *lamin B receptor* (*Lbr*) knock out (KO) mouse thymocytes, which lack both lamin A/C and LBR, exhibit detachment of heterochromatin from the nuclear periphery, the A/B compartment pattern remains unaffected mainly (7). Furthermore, the depletion of RIF1, the master regulator of replication timing (RT), had a limited effect, as we did not observe a compartmental pattern failure parallel to the induced RT failure (8). Thus, the NL association and RT are not essential for A/B compartment determination.

The epigenetic hallmark of heterochromatin, particularly constitutive heterochromatin, is the trimethylation of histone H3 lysine 9 (H3K9me3). Heterochromatin protein 1 (HP1) is a reader molecule for H3K9 methylation; it condenses chromatin (9–13) and drives B compartment formation in *Drosophila* embryos (14). In mammals, at least five enzymes—SUV39H1, SUV39H2, SETDB1, G9a and GLP–contribute to the catalysis of H3K9 methylation. SUV39H1, SUV39H2 and SETDB1 mainly catalyze H3K9me3 formation, whereas H3K9me2 formation is regulated by all five enzymes (15,16). Recently, we investigated the role of H3K9 methylation in A/B compartment formation using *Setdb1* KO or *Suv39h1/2* double KO (DKO) mouse embryonic stem cells (mESCs) treated with UNC0642, a G9a/GLP specific inhibitor (16). We found that these cells maintained an overall A/B compartment pattern regardless of the global reduction in H3K9 methylation (16). However, it is still possible that H3K9 methylation plays a more crucial role in A/B compartment formation because H3K9 methylation, especially that other than H3K9me3, remained in the analyzed cells owing to the incomplete depletion of H3K9 methylation (16). Alternatively, other epigenetic modifications (s) may compensate for the role of H3K9 methylation in A/B compartment formation in the analyzed cells. H3K27me3 is another silencing mark, especially for facultative heterochromatin, such as silenced cell type-specific genes and the inactive X chromosome (1). Although H3K27me3 and H3K9me3 normally exist separately along the chromosome, H3K27me3 invades H3K9me3-marked heterochromatin regions when H3K9me3 is depleted by perturbing the H3K9me3 pathway (17,18). Thus, H3K27me3 may compensate for the function of H3K9me3 in heterochromatin organization after the loss of H3K9 methylation.

Recently, Montavon *et al.* reported that conditional loss of H3K9 methylation in immortalized mouse embryonic fibroblasts (iMEFs) deficient in H3K9 methyltransferase genes (*Suv391h, Suv39h2, Setdb1, Setdb2, Ehmt1/GLP* and *Ehmt2/G9a*) results in the loss of heterochromatin, as observed by electron microscopy (EM) (15). However, whether H3K9 methylation is required for the spatial arrangement of heterochromatin and A/B compartmentalization in mammals remains to be discovered, as these studies did not analyze 3D genome organization in H3K9 methylation-depleted cells. Also, the possibility that H3K27me3 partially compensates for the absence of H3K9me3 remains unclear.

To address whether repressive chromatin modifications such as H3K9me2/3 and H3K27me3 play essential roles in the spatial arrangement of heterochromatin, we independently established 5KO iMEFs (*Suv391h, Suv39h2, Setdb1, Ehmt1* and *Ehmt2 KOs*) that completely lack H3K9 methylation. Because 5KO iMEFs are viable, they provide a unique opportunity to explore the plasticity of heterochromatin organization in mammals. To investigate the roles of H3K9me2/3 and H3K27me3 in the spatial organization of heterochromatin, we performed *in situ* Hi-C, and lamin A/C and lamin B1 ChIP-seq in wild type and 5KO iMEFs treated with or without DS3201, an H3K27 methyltransferase inhibitor. We found that condensation and spatial arrangement of heterochromatin were not greatly impaired in 5KO cells but underwent major changes when the cells were treated with DS3201. Thus, the H3K27me3 pathway compensates for the function of H3K9me2/3 in heterochromatin organization after the loss of H3K9 methylation. In other words, the H3K9me2/3-marked heterochromatin organization can be redundantly maintained by either the H3K9 or the H3K27 methylation axis in mammals.

MATERIALS AND METHODS

Cell culture

We used previously established *Setdb1, Suv39h1/2* TKO iMEFs to establish 5KO iMEFs (16). Mouse embryonic fibroblasts were maintained in Dulbecco's modified Eagle's medium (Nacalai tesque, 08458–16) containing 10% fetal bovine serum (Biosera, FB1061), MEM non-essential medium and 2-mercaptoethanol (Nacalai tesque, 21417-52). To inhibit EZH1/2 catalytic activity, iMEFs were cultured for seven days with 1 μM DS3201 (Selleck, S8926).

Establishment of 5KO and 5KO + *Ring1b* KO iMEFs

Setdb1/Suv39h1/2 TKO iMEFs were transfected with PL-CRISPR.EFS.tRFP with gRNA sequences targeting SET-domain of *G9a* or *Glp*. 2 days after the transfection, RFP positive cells were sorted by flow cytometry (BD FACSAria). From the sorted cells, 5KO iMEF clones were identified using Sanger sequencing and western blotting. Further knockout of *Ring1b* in 5KO iMEFs were conducted by similar protocols.

Ring1a knockdown by shRNA

We produced a lentiviral vector expressing shRNA targeting *Ring1a* by transfecting 293FT cells with shRNA vector, psPax2, and pMD2.G using PEI. Two days later, we collected the culture supernatant and then used it to transduce 5KO-*Ring1b* KO iMEFs at MOI = 2. Following selection with 7 μg/ml BSD for 3 days, we collected the cells.

Native ChIP and crosslinked ChIP

Native ChIP assays were performed as described previously (16). Mouse monoclonal antibody against H3K9me3 (2F3), H3K9me2 (6D11), H3K27me3 (1E7), lamin A/C (3A6-4C11, eBioscience) and lamin B1 (B-10, sc-374015, Santa Cruz) were used.

H2AK119 monoubiquitylation (H2Aub) carrier assisted ChIP-seq (CATCH-seq)

H2Aub CATCH-seq libraries were prepared as previously described (Zhu *et al.*, 2021) with some modifications. Briefly, 2000 MEFs per sample were used for library construction. Cells were permeabilized by Nuclei EZ lysis buffer supplemented with 0.1% Triton, 0.1% deoxycholate, complete EDTA-free protease inhibitor cocktail and 1 mM phenylmethanesulfonyl fluoride on ice. For each sample, 800 S2 Drosophila culture cells were added for a spike-in normalization purpose. Chromatin was fragmented *in situ* by 2 U/μl MNase (M0247S, NEB) at 37C for 7.5 min. The reaction was stopped by adding 1/10 volume of 100 mM EDTA and diluted in the freshly prepared immunoprecipitation buffer. As an input, 5% of the chromatin lysate was taken. Then, 30 ng of annealed I-SceI carrier DNA was added to each sample. The forward and reverse strands of the carrier DNA were as follows:

/5AmMC6/Gtagggataacagggtaattagggataacagg gtaattagggataacagggtaattagggataacagggtaattagggat aacagggtaattagggat aacagggtaat*c/3AmMO/ and /5AmMC6/Gattaccctgttatccctaattaccctgttatccctaattaccctg ttatccctaattaccctgttatccctaattaccctgttatccctaattaccctgttatcc cta*c/3AmMO/, respectively, where asterisks represent phosphorothioate bonds. The oligos were synthesized by Integrated DNA Technologies. For each immunoprecipitation reaction, 0.5 μl of rabbit monoclonal anti-H2AK119 monoubiquitylation antibody (Cell Signaling, #8240) conjugated to precleared Dynabeads Protein A and G mixture was used. After immunoprecipitation at 4°C overnight, the chromatin-Dynabeads were washed by the low and high salt wash buffers, and the chromatin was eluted in the freshly prepared ChIP elution buffer at 65C for 1 h. DNA was recovered by phenol-chloroform extraction followed by ethanol precipitation. Adaptor ligation was pre-formed by NEBNext Ultra II DNA Library Prep Kit for Illumina (E7645, NEB) in a half scale of the manufacturer's instruction, and the libraries were purified by 1.8× SPRIselect beads (B23318, Beckman Coulter). The DNA was amplified by KAPA Hifi 2X mater PCR mix (KK2605) for 14 PCR cycles with indexing primers. After purification with 0.9× SPRIselect beads, the samples were digested by I-SceI (5 U/μl, NEB, R0694) 37C for 2 h followed by heat inactivation at 65°C for 20 min and purified by 0.9× SPRIselect beads. The second amplification was not performed. The libraries were sequenced on a HiSeq X.

Western blot analysis

Western blot analysis was performed as described previously (16). Briefly, cells were suspended in RIPA buffer (50 mM Tris–HCl (pH 8.0), 420 mM NaCl, 0.5% sodium deoxycholate, 0.1% Sodium dodecyl sulfate, 1% NP-40) and sonicated. The extract was incubated for 30 min on ice, and then incubated at 95°C for 5 min. The extract was loaded and run on SDS-PAGE gel as standard protocols. For histone proteins, intensity was analyzed by OdysseyR CLx Imagins System(LI-COR). Anti-lamin B1 (12987-1-AP, Proteintech), anti-lamin A/C (3A6-4C11, Diagenode), anti-H2Aub (D27C4), anti-Ring1B (monoclonal antibody kindly gifted from Dr Koseki, RIKEN), anti-Ring1A (#2820, CST) were used.

Mass spectrometry analysis for histone modifications

Histones were prepared by the acid-extraction method as previously described (16). The samples were subjected to SDS-PAGE and stained with Coomassie blue. The protein bands corresponding to histone H3 were excised from the gel and were digested with *Achromobacter* protease I (Lys-C) in gel. The digests were performed nano-liquid chromatography–tandem mass spectrometry using EASY-nLC 1200 liquid chromatography (Thermo Fisher Scientific) connected to Q-Exactive HFX mass spectrometer equipped with nanospray ion source (Thermo Fisher Scientific). Peptides containing the digests were separated with a linear gradient of 0–100% B buffer in A buffer (A:0.1% formic acid, B:80%acetonitrile/0.1%formic acid) for 20 min with a reversed-phase column (NTCC analytical column, C18, φ75 μm × 150 mm, 3 μm; Nikkyo Technos, Japan). MS and MS/MS data were acquired using a data-dependent TOP 10 method. Protein quantification was performed with Proteome Discoverer 2.4. (Thermo Fisher Scientific) using a sequence database search node as a MASCOT program 2.7 (Matrix Science) with following parameters, Database: Histone 130611 (66 sequences; 15002 residues), Enzyme: Lys-C/P, Variable modifications: Acetyl (Protein Nterm), Oxidation (M),Gln→pyro-Glu (N-term Q),Acetyl (K),Methyl (K),Trimethyl (K),Dimethyl (K), Mass values: Monoisotopic, Protein Mass: Unrestricted, Peptide Mass Tolerance: ±15 ppm, Fragment Mass Tolerance: ±30 mmu, Max Missed Cleavages: 3, Instrument type: ESI-TRAP. Protein methylation rates were obtained from peak areas of selected

ion chromatograms that are the tetra charged protonated molecules at m/z 381.9706 (Q5 pyro-Glu, K9monomethyl and K14Actryl), *m/z* 385.4745 (Q5 pyro-Glu, K9dimethyl and K14Actryl), and *m/z* 388.9784 (Q5 pyro-Glu, K9trimethyl and K14Actryl) of 'QTARKSTGGKAPRK'-related peptides and at *m/z* 604.3548 (K23Acetyl and K27monomethyl), *m/z* 609.0267 (K23Acetyl and K27dimethyl), and *m/z* 613.6985 (K23Acety and K27trimethyl) of 'QLATKAARKSAPATGGVK'-related peptides using Qual Browser (Thermo xcalibur 4.1.50, Thermo Fisher Scientific) with ±15-ppm width.

Indirect immunofluorescence

Cells were grown on μ-Dish 35 mm dish high (ibidi) and were fixed with 4% PFA (Electron Microscopy Sciences) in PBS (FUJIFILM Wako) containing 250 mM HEPES-NaOH (pH 7.4, Nacalai Tesque) + 0.1% Triton X-100 (Nacalai Tesque) at room temperature for 10 min, followed by permeabilization with 1% Triton X-100 in PBS containing Blocking One P (Nacalai Tesque) at room temperature for 30 min. The processed cells were incubated with primary lamin A/C Monoclonal Antibody (1:5000, 3A6-4C11, eBioscience), primary lamin B1 Monoclonal Antibody (1:100, B-10, sc-374015, Santa Cruz) and primary lamin A polyclonal antibody (1:2000, 323-10), which was kindly provided by Dr Robert D. Goldman in Northwestern University in PBS containing 10% Blocking One P at 4°C overnight. After washes with PBS containing 0.05% Tween 20 (FUJIFILM Wako) three times, the cells were incubated with 1 μg/ml Hoechst 33342 (1:10 000, Thermo Fisher Scientific) and Donkey anti-Mouse IgG (H + L) Highly Cross-Adsorbed Secondary Antibody, Alexa Fluor 488 (1:1000, Thermo Fisher Scientific) and Alexa Fluor 568 (1:1000, Thermo Fisher Scientific) in PBS containing 10% Blocking One P. After washing three times, 2 ml of PBS was added to the dish.

Fluorescence microscopy

Cells were observed using a confocal microscope, which is Ti-E (Nikon) equipped with Dragonfly 200 (Andor) and an oil immersion objective lens (CFI HP Plan Apochromat VC 100× Oil, NA = 1.4, Nikon) and operated by built-in software Fusion ver. 2.3.0.45 (Andor). The images were collected with an EMCCD camera (iXon Life 888, Andor) with 10% 405 nm laser transmission, 500 ms, and 30% 488-nm laser transmission, 300 ms. For z-stack image acquisition, optical sections including a region of the NL were taken at 0.6-μm intervals. Enlarged lamin meshes were automatically detected using Aivia's 3D cell analysis recipe in Aivia verion 10.5 (SVision Technologies), and the results were validated by visual inspection. First, a random forest pixel classifier for detecting enlarged meshes was trained by selecting enlarged meshes and removing background signals in the lamin channel of five images of 5KO #55 iMEF, and deselecting normal meshes in the lamin channel of five images of WT iMEF. Then, this classifier was used to generate the confidence channel with a range between 0 (least likelihood of belonging) and 255 (most likelihood of belonging). Next, the Hoechst and confidence channels were used to generate object sets of nuclei and meshes, respectively with the recipe parameters including image smoothing filter size in morphological smoothing: 5 and fill holes size: 250 μm^2 for nuclei, and cells/vesicles diameter: 6−30 μm/0.6−1 μm and min edge to center distance: 6 μm/0.4 μm for nuclei/meshes. Then, nuclei with one or more meshes were counted in all the images.

Chromocenter analysis

Identification and analysis of chromocenters were automatically conducted by NODeJ (19) by the following options: -gx = 1, -gy = 1, -gz = 0.5, -max = 500, -min = 5, -f = 1.5, -isF, -isG. More than 50 cells were used for the analysis for each sample.

EM imaging and data analysis

Cells were fixed with 2.5% glutaraldehyde and 2% paraformaldehyde in 0.1M HEPES buffer (pH 7.4) at room temperature for 1 h and then at 4°C. After washing five times with 0.15 M sodium cacodylate buffer, they were postfixed with 1% osmium tetroxide in the same buffer at 4°C for 1 h and then washed five times with Milli-Q water. Cells were further incubated in 1% uranyl acetate at 4°C for 1 h, washed five times with Milli-Q water, and dehydrated with an ethanol series (20, 50, 70, 90 and 99.5% for 5 min each and twice in 100% for 10 min) followed by infiltration with Epon 812 resin (TAAB). Polymerization was performed at 60°C for 72 h. Samples were cut using an EM UC7 ultramicrotome (Leica Biosystems). Sections 60nm in thickness were stained with uranyl acetate and lead nitrate. Electron micrographs were acquired using a field emission scanning electron microscope JSM-7900F and JSM-IT700HR (JEOL) at 7kV.

Electron-dense heterochromatin regions in nuclei were analyzed using ImageJ version 1.53c (https://imagej.nih.gov/ij/). EM images were Gaussian blurred (sigma 2) and electron-dense heterochromatin was selected by thresholding based on the intensity levels (87–141, depending on the images) and the size (>400 pixels). Nucleolar regions were often selected together with heterochromatin and were manually excluded, since they can be distinguishable from heterochromatin based on their larger size and the presence of different components, including granular component that shows slightly less electron density than heterochromatin and dense fibrillar component that shows similar electron density to heterochromatin but often associated with less dense fibrillar components. The nuclear envelope was difficult to separate from the perinuclear heterochromatin and so included in heterochromatin area. The ratio of heterochromatin area respect to the nuclear area, which was selected manually, was determined for 10 cells.

Visualization of major satellite by TALE probe

A plasmid vector for EGFP-tagged TALE probe targeting Major satellite was used. The TALE probe targets (T) GATTTTCAGTTTTCT sequence (20). We established stable WT (#3–12) and 5KO (#55) iMEFs expressing the

TALE probe using PiggyBac system. The cells were incubated with 10 μg/ml Hoechst 33342 (1:2000, Dojinbo) and observed by FV3000 (Olympus).

Preparation of ChIP-seq library

The ChIP DNA was fragmented by Picoruptor (Diagenode) for 10 cycles of 30 s on, 30 s off. Then, ChIP library was constructed by KAPA Hyper Prep Kit (KAPA BIOSYSTEMS) and SeqCap Adapter Kit A (Roche) according to manufacturer instructions. The concentration of the ChIP-seq library was quantified by KAPA Library quantification kit (KAPA BIOSYSTEMS). ChIP sequencing was performed on a HiSeq X platform (Illumina). We performed two biological replicates for ChIP-seq and correlation between replicates was described in Supplementary Table 1.

Preparation of RNA-seq library

500 ng of total RNA was used for RNA-seq library construction. RNA-seq library was constructed by KAPA mRNA Hyper Prep Kit (KAPA BIOSYSTEMS) and SeqCap Adapter Kit (Roche) according to manufacturer instructions. The concentration of the RNA-seq library was quantified by KAPA Library quantification kit (KAPA BIOSYSTEMS). mRNA sequencing was performed on a HiSeq X platform (Illumina). We performed two biological replicate for RNA-seq and correlation between replicates was described in Supplementary Table 1.

Preparation of Hi-C library

Hi-C experiments were performed as previously described (21,22), based on DpnII enzyme (4-bps cutter) using 2×10^6 fixed cells. Hi-C libraries were subject to paired-end sequencing (150 base pair (bp) read length) using HiSeq X Ten. Detailed protocol for HiC-seq library preparation is available at Protocols.io (https://www.protocols.io/view/iconhi-c-protocol-ver-1-0-4mjgu4n). We performed two biological replicates for Hi-C seq and correlation between replicates was described in Supplementary Table 1.

Preparation of WGBS library

500 ng of genomic DNA was sheared by sonication to 100–500 bp using a Covaris S220 and purified by AMPure XP beads (Agencourt Bioscience Corp.). Genomic DNA libraries were constructed as ChIP-seq library. After adapter ligation, the DNA was treated with sodium bisulfite using EZ DNA Methylation GOLD kit (ZYMO RESEARCH) following the manufacturer's instructions. Enrichment for adapter-ligated DNA was carried out through 10 PCR cycles using Pfu Turbo Cx Hotstart DNA polymerase (Agilent). The concentration of the WGBS library was quantified by KAPA Library quantification kit (KAPA BIOSYSTEMS). Paired-end DNA sequencing (2 × 150 bp) was then performed using the Illumina Hi-Seq X plat form (Illumina). We performed two biological replicate for WGBS and correlation between replicates was described in Supplementary Table 1.

Hi-C data analysis

Hi-C data processing was done by using Docker for 4DN Hi-C pipeline (v43, https://github.com/4dn-dcic/docker-4dn-hic). The pipeline includes alignment (using the mouse genome, mm10) and filtering steps. After filtering valid Hi-C alignments, *.hic* format Hi-C matrix files were generated by Juicer Tools (23) using the reads with MAPQ >10. The A/B compartment (compartment score) profiles (in 250 kb bins) in each chromosome (without sex chromosome) were calculated from *.Hic* format Hi-C matrix files (intrachromosomal KR normalized Hi-C maps) by Juicer Tools (23) as previously described (24). We averaged Hi-C PC1 values in each 250 kb bin from two biological replicates for the downstream analysis. TAD boundaries were identified as previously reported (25). Chromatin loops were identified by SIP, Significant Interaction Peak caller, v1.6.1 (26) with the following parameters: -norm KR -g 0.5 -min 2.0 -max 2.0 -mat 2000 -d 5 -res 40 000 -sat 0.01 -t 2800 -nbZero 6 -factor 1 -fdr 0.015 -del true -cpu 1 -isDroso false. We used GENOVA tools (27) for producing aggregate TAD plots, insulation analysis and pyramid plots. We also used Juicer Tools (23) for producing interaction matrix and Pearson correlation matrix.

Identification of TAD boundary

Insulation score was calculated in each 40 kb bin by GENOVA tools, then local minimum search within 120 kb was performed. We assigned 40-kb bins with local minimum to TAD boundaries if the score differences between bins local minimum and bins with local maxima was greater than 0.3. In this condition, we got a high reproducibility of TAD boundary between biological replicates (>88%).

Clustering of genomic regions by chromatin modifications

Log_2(ChIP/Input) of H3K9me3 in WT iMEFs and H3K27me3 in WT and 5KO iMEFs, and average DNA methylation levels in WT and 5KO iMEFs were calculated in each 250 kb bin. Next, each bin was classified to A or B compartment using Hi-C PC1 values from WT iMEFs. *k*-means clustering with $k = 5$ was performed on A and B compartment, independently by kmeans function in R.

Interaction between TAD type

We assigned the cluster that occupies the most space to the TAD. The observed/expected values of interaction frequency between 40 kb bins were obtained by Dump function in Juicer Tools (23). The observed/expected values were averaged for each TAD combination. Then, we further averaged the values for each TAD type combination to produce heatmap in Figure 3C.

ChIP-seq analysis

Adaptor sequences and low quality bases in reads were trimmed using Trim Galore version 0.3.7 (http://www.bioinformatics.babraham.ac.uk/projects/trim_galore/). Then trimmed reads were aligned to the mouse GRCm38 genome assembly using bowtie version 0.12.7 (28) with

default parameters. Duplicated reads were removed using samtools version 0.1.18 (29).

RNA-seq analysis

Adaptor sequences and low quality bases in reads were trimmed using Trim Galore version 0.3.7 (http://www.bioinformatics.babraham.ac.uk/projects/trim_galore/). To calculate RPM values in each 250 kb bin, trimmed reads were aligned to the mm10 genome build using bowtie version 0.12.7 with –m 1. Duplicated reads were removed using samtools version 0.1.18. The number of mapped reads in each 250 kb bin was counted by featureCounts (30), then, RPM values in each 250 kb bin was calculated. To identify differentially expressed genes or repeats, the trimmed reads were mapped to the mouse GRCm38 genome assembly using TopHat (v2.1.1) with –g 1 (31). After read mapping, the number of reads mapped in genes or repeats was counted by TEtranscripts (v1.4.11) with default parameters) (32). We performed two biological replicates for RNA-seq and identified DE genes and repeats by DESeq2 (adj. P-value < 0.05, FC > 2) (33).

WGBS analysis

Adaptor sequences and low quality bases in reads were trimmed using Trim Galore version 0.3.7 (http://www.bioinformatics.babraham.ac.uk/projects/trim_galore/). The trimmed reads were mapped to the mouse GRCm38 genome assembly using Bismark v0.14.1 with single-end and non-directional mapping parameters (34). The methylation level of each CpG site was calculated as follows: number of methylated reads/number of total reads. To calculate DNA methylation levels in each 250 kb bin, we averaged the DNA methylation levels of CpG sites within a bin. We performed two biological replicates for WGBS and averaged methylation levels between the replicates in each 250-kb bin was used for the downstream analysis.

Visualization of NGS data

The Integrative Genomics Viewer (IGV) (35) was used to visualize NGS data. For Hi-C contact matrix and correlation matrix, we used Juicer Tools (23).

Statistical analysis

All methods for statistical analysis and P-values in this study are described in each figure legend and included in each figure, respectively.

RESULTS

Establishment of H3K9 methylation complete deficient iMEFs

We previously established *Setdb1, Suv39h1* and *Suv39h2* triple-KO (TKO) iMEFs lacking H3K9me3 (16). To establish a cell line with complete loss of H3K9 methylation, we introduced Cas9 and gRNAs targeting exon 26 of *Ehmt1* and *Ehmt2,* which encode the SET domain of GLP or G9a, respectively, into TKO iMEFs (Supplementary Figure S1a) and isolated four clones with compound mutations for all five H3K9 methyltransferases (5 KO iMEFs). Western blot and DNA sequencing analyses validated *Ehmt1* and *Ehmt2* KO (Supplementary Figure S1b, c). We confirmed that H3K9 methylation was undetectable in 5KO iMEFs using western blot and mass spectrometry (MS) analyses (Supplementary Figure S1d, e).

The most prominent heterochromatin domains in mice are formed across major satellite repeats around centromeric regions called pericentromeres. Pericentromeric heterochromatin regions can form clusters in interphase nuclei, termed chromocenters, which can be visualized using nucleic acid staining reagents such as Hoechst 33342 and DAPI. When we applied this method to cells expressing a TALE probe specific for major satellite repeats (20), we found no apparent differences in the Hoechst dense pattern of major satellite repeats between WT and 5KO cells (Supplementary Figure S1f). We also performed EM to determine whether electron-dense heterochromatin was present in the nuclei of WT, TKO and 5KO iMEFs. We found heterochromatin at the nuclear periphery in the WT, TKO, and 5KO iMEFs, although one of the 5KO iMEF clones (#55) appeared to have less heterochromatin (Supplementary Figure S1g; see below for quantitative analysis). These results suggest that heterochromatin organization is largely maintained even without H3K9 methylation.

Redistribution of H3K27me3 after the loss of H3K9 methylation

To verify whether other repressive chromatin modifications contribute to heterochromatin formation in the H3K9me2/3-marked regions after the inactivation of all H3K9 methyltransferases, we analyzed DNA methylation, H3K9me2/3, and H3K27me3 in WT and 5KO iMEFs by whole-genome bisulfite sequencing (WGBS) and ChIP-seq, respectively. We observed that H3K9me3 and H3K27me3 were segregated (Figure 1A), and although their respective modification intensities were strongly inversely correlated (Figure 1B, left panel), analysis at a 250 kb bin resolution indicated that relatively high levels of H3K27me3 were present in the H3K9me3 positive B compartment regions. Moreover, the extent of H3K27me3 enrichment in the H3K9me3-marked B compartment regions was increased in 5KO iMEFs. In contrast, DNA methylation levels were significantly decreased in both A and B compartments, with a more significant reduction observed in compartment B (Figure 1A, B). In the B compartments of WT iMEFs, H3K9me3 increased with distance from the A/B boundary, peaked approximately 1.5 Mb away, and remained at high levels, whereas H3K27me3 was the highest near the A/B boundary, decreased as the distance increased, reached its lowest level at approximately 1 Mb from the boundary, and maintained a low level further away from the boundary (Figure 1C). In contrast, in the 5KO iMEFs, where H3K9 methylation was absent, the decrease in H3K27me3 away from the boundary became shallow, reaching a minimum of approximately 2.5 Mb away; however, this reduction was not evident in the B compartments at greater distances (Figure 1C). RNA-seq analysis of WT and 5KO iMEFs revealed that the transcribed regions

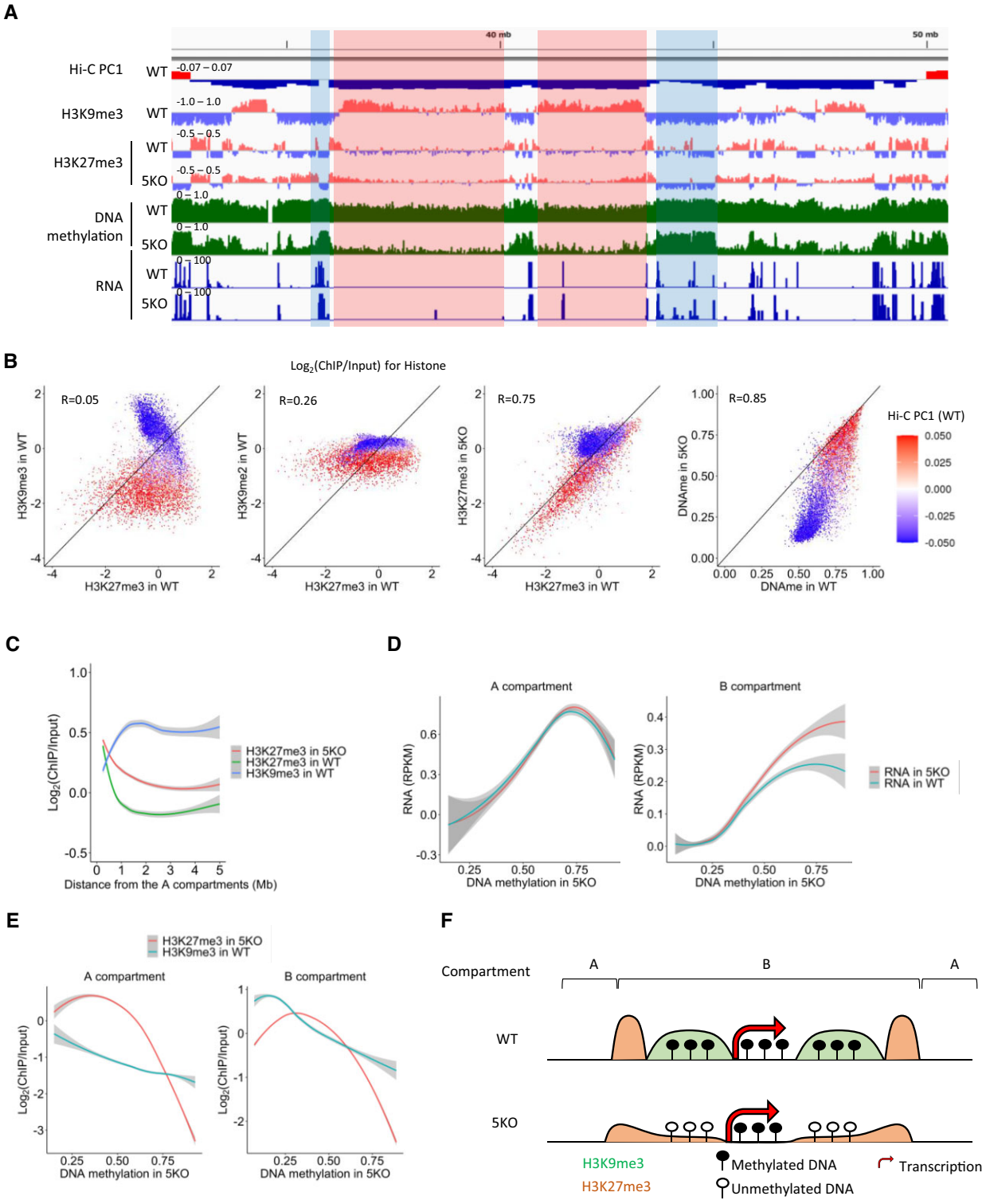

Figure 1. Redistribution of H3K27me3 after the loss of H3K9 methylation. (**A**) Representative view of invading H3K27me3 to regions targeted by H3K9me3 after the loss of H3K9 methylation. The regions highlighted by red and blue represent invasion of H3K27me3 and transcription-associated maintenance of DNA methylation, respectively. (**B**) Scatter plots of correlation between H3K9me3 or H3K9me2 and H3K27me3 enrichment in WT iMEFs, and H3K27me3 enrichment or DNA methylation levels between WT and 5KO iMEFs in each 250 kb bin. Each plot is colored by Hi-C PC1 value in WT iMEFs. (**C**) LOESS smoothing line plots between distance from the A compartments and enrichment of H3K9me3 in WT iMEFs, H3K27me3 in WT iMEFs and H3K27me3 in 5KO iMEFs. Data from each 250 kb bin in the B compartments was used for this analysis. (**D**) LOESS smoothing line plots between DNA methylation levels in 5KO iMEFs and RNA expression in WT iMEFs or 5KO iMEFs. DNA methylation levels in 5KO iMEFs was positively correlated with RNA expression levels in both WT and 5KO iMEFs. (**E**) LOESS smoothing line plots between DNA methylation levels in 5KO iMEFs and enrichment of H3K27me3 in 5KO or H3K9me3 in WT iMEFs. DNA methylation levels in 5KO iMEFs was negatively correlated with H3K27me3 and H3K9me3 enrichment. (**F**) Summary of epigenome profiles in the B compartments after the loss of H3K9 methylation.

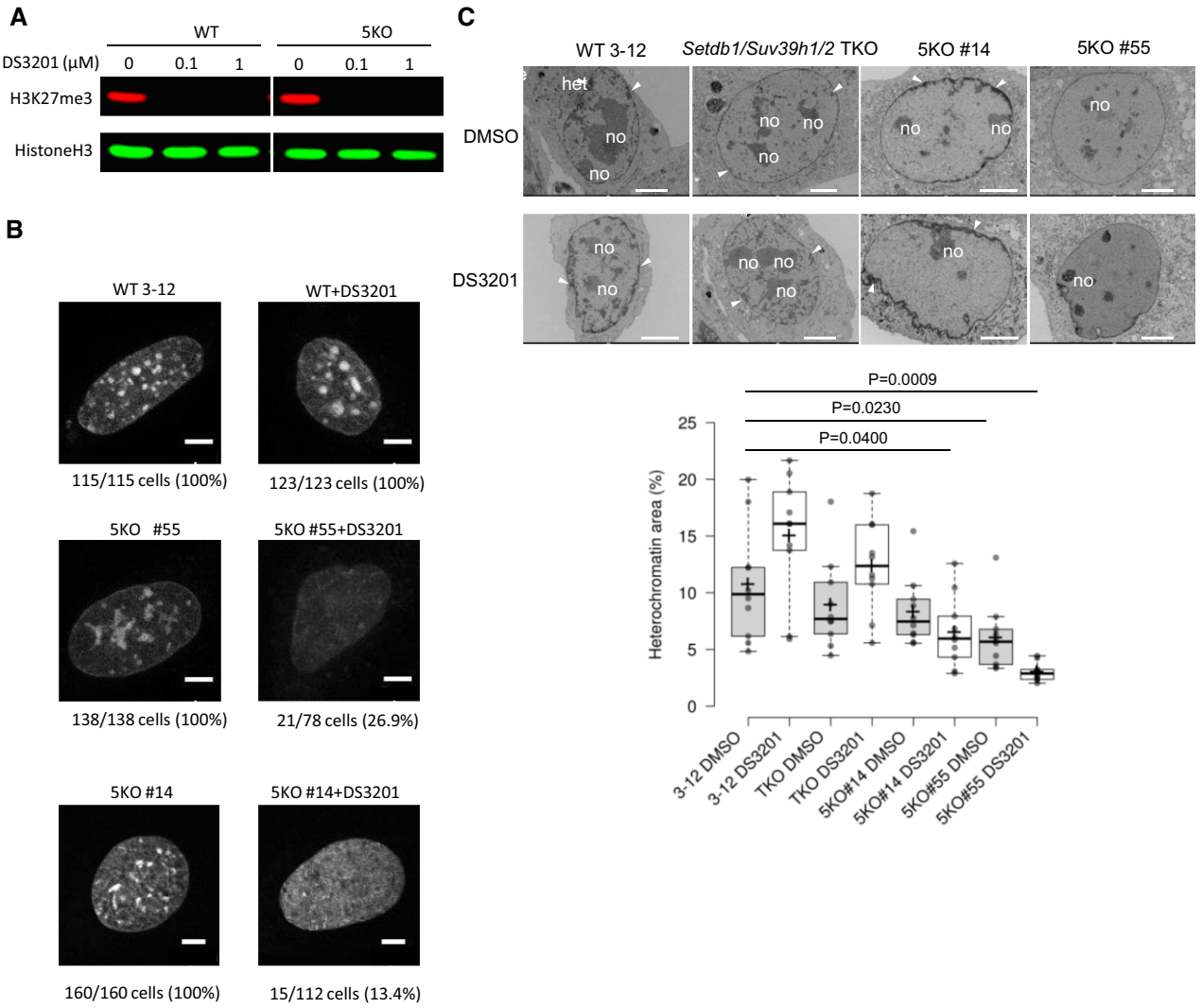

Figure 2. Impairment of heterochromatin organization by the depletion of both H3K9 and H3K27 methylation. (**A**) Western blotting analysis of H3K27me3 in WT and 5KO iMEFs treated with or without DS3201 for 7 days. (**B**) Hoechst staining in WT and 5KO iMEFs treated with or without 1 μM DS3201 for 7 days. 26.9% of DS3201-treated 5KO iMEFs showed loss of chromocenters. A scale bar (5 μm) is indicated in each micrograph. (**C**) EM analysis in WT (3–12), TKO and 5KO (#14 and #55) iMEFs treated with or without 1 μM DS3201 for 7 days. Some nucleoli are indicated as 'no'. Arrowhead indicates electron-dense heterochromatin. A scale bar (5μm) is indicated in each micrograph. In the box plots ($n = 10$ each), the medians are shown by center lines. Box limits indicate the 25th and 75th percentiles and whiskers extend 1.5 times the interquartile range from the 25th and 75th percentiles. P values < 0.05 by Student's t-test (unpaired, two-tailed) are indicated.

in the B compartments had higher DNA methylation in 5KO than WT iMEFs (Figure 1D), and these highly DNA methylated regions had low H3K9me3 levels in WT iMEFs and low H3K27me3 levels in 5KO iMEFs (Figure 1E). Although resistance against H3K27me3 invasion inside the transcribed B-compartment regions existed (Figure 1A, F), the redistribution of H3K27me3 into the B-compartments in 5KO iMEFs prompted us to investigate the function of H3K27me3 in H3K9me2/3-marked heterochromatin organization after the loss of H3K9 methylation.

Loss of both H3K9me2/3 and H3K27me3 impaired heterochromatin organization

For this purpose, we used DS3201, which has been reported to effectively inhibit the H3K27 methyltransferase EZH1/2 (36). Western blotting and mass spectrometry analyses confirmed that treatment of 5KO iMEFs with 1 μM DS3201 for 7 days reduced H3K27me3 and H3K27me2 levels to less than 0.2% and 1.6%, respectively, compared to untreated cells (Figure 2A, Supplementary Figure S2). Despite losing H3K9 and H3K27 methylation, DS3201 treatment did not affect cell growth in 5KO iMEFs (Supplementary Figure S3a). First, we investigated the effect of H3K9 and H3K27 methylation loss on the transcriptome using RNA-seq analysis with two biological replicates in WT and 5KO iMEFs treated with or without DS3201. We confirmed the reproducibility of gene expression profiles using principal component analysis (PCA) (Supplementary Figure S3b). Differentially expressed genes and repeats in each sample identified by TEtranscripts (FDR < 0.05, $\log_2(FC) > 1$) (32) showed that the most significant number

of genes and repeats were dysregulated in DS3201-treated 5KO iMEFs among all samples (Supplementary Figure S3c) and that 40.4% (1167/2887) and 37.7% (447/1183) of up- and down-regulated genes in DS3201-treated 5KO iMEFs were specific to this condition (Supplementary Figure S3d). Thus, the H3K9 and H3K27 methylation pathways cooperatively regulate both genes and repeats. We also found that the *Zscan4* gene cluster was upregulated only in DS3201-treated 5KO iMEFs and that H3K27me3 was enriched over the cluster region in 5KO iMEFs but not in WT iMEFs (Supplementary Figure S3e). This result suggests that H3K27me3 redistribution compensates for H3K9 methylation-mediated gene silencing after the loss of H3K9 methylation.

Next, to investigate whether heterochromatin organization was impaired by removing H3K27me3 from 5KO iMEFs, we performed Hoechst 33342 staining of WT and 5KO iMEFs treated with DS3201. A total of 13.4% (#14) to 27.0% (#55) of DS3201-treated 5KO iMEFs showed loss or drastically decreased chromocenter formation, whereas the chromocenter was maintained in DS3201-treated WT iMEFs (Figure 2B). Automated analysis of chromocenters using NODeJ (19) also showed a decrease in the number, volume, and intensity of chromocenters in DS3201-treated 5KO iMEFs (Supplementary Figure S4a–c). We also performed EM analysis to examine how electron-dense heterochromatin regions in the nucleus were affected by DS3201 treatment in WT, TKO, and 5KO iMEFs (Figure 2C). The areas of electron-dense heterochromatin regions in the nuclei were 11% and 9.0% in WT and TKO iMEFs, respectively, and increased to 15% and 12%, respectively, upon DS3201 treatment. In the 5KO iMEFs clones, heterochromatin regions (8.3% and 6.0% in #14 and #55, respectively) significantly decreased to 6.5% and 3.0%, respectively, upon treatment with DS3201 (Figure 2C). Thus, heterochromatin condensation is significantly impaired by the loss of both H3K9me2/3 and H3K27me3.

We further validated how much transcriptional regulation is important for the compensation function of the redistributed H3K27me3 to the heterochromatin formation after the loss of H3K9 methylation. We found that H3K27me3 enrichment in 5KO iMEFs, which is largely different from that in WT iMEFs, was more strongly correlated with differences in Hi-C PC1 values between 5KO + DS and 5KO than with RNA expression differences between 5KO + DS and 5KO (Supplementary Figure S5). Moreover, linear model analysis of changes in Hi-C PC1 values between 5KO and 5KO + DS, based on RNA expression changes ($\log_2$(FC)) and H3K27me3 accumulation in 5KO, revealed that expression changes explained only 9% of the PC1 Hi-C variation. In comparison, H3K27me3 accumulation explained over 30%. Therefore, we conclude that the contribution through transcriptional regulation in maintaining heterochromatin formation carried by the redistributed H3K27me3 is limited, if any.

Deformation of the nuclear lamina in 5KO iMEFs

We also examined nuclear lamina formation in H3K9 and H3K9 + H3K27 methylation-depleted 5KO iMEFs because, as reported recently, deformation of nuclear lamina was described in H3K9 depleted iMEFs (15). The lamin A/C meshwork of the nuclear lamina in WT, *Setdb1* KO, *Setdb1*/*Suv39h1*/*Suv39h2* TKO, and 5 KO (#14 and #55) iMEFs were examined using indirect immunofluorescence. The proportion of TKO and 5KO iMEF nuclei with enlarged lamin meshes was higher than that of the WT iMEF nuclei (Supplementary Figure S6a). These structural alterations in the nuclear lamina were similar to those found in lamin A/C- or lamin B1-depleted cells (37,38) without a decrease in the expression levels of these lamins in 5KO iMEFs (Supplemental Figure S6b). In contrast to the 5KO iMEFs, the enlarged mesh of *Setdb1* KO iMEF nuclei was less evident than that of WT iMEF nuclei (Supplementary Figure S6a), which is a bit inconsistent with a previous report (15). Next, when WT and 5KO #55 MEFs were treated with DS3201, the proportion of 5KO MEFs positive for the enlargement of mesh size increased by approximately two-fold compared to control iMEFs treated with DMSO (Supplementary Figure S6c); this effect was not observed in WT iMEFs. Finally, we examined whether the lamin B1 meshwork was also affected in 5KO iMEFs, as seen for the lamin A/C meshwork, and found that the lamin B1 meshwork was similarly affected in 5KO iMEFs with or without DS3201 treatment (Supplementary Figure S6d). These results indicate that the loss of H3K9 and H3K9me3 + H3K27 methylation causes heterochromatin impairment and deformation of the nuclear lamina. Simultaneously, we cannot rule out that lamina disruption is the main driver of changes in heterochromatin organization.

Loss of both H3K9me2/3 and H3K27me3 reduced heterochromatin-euchromatin segregation

To further investigate the impairment of heterochromatin organization in DS3201-treated 5KO iMEFs, we performed *in situ* Hi-C analysis of WT and 5KO (#55) iMEFs treated with or without DS3201. DS3201-treated 5KO iMEFs showed weakened compartmentalization (Figure 3A) and a weakened bimodal pattern of Hi-C PC1 values (Supplementary Figure S7a), suggesting segregation of the B compartment from the A compartment was weakened in DS3201-treated 5KO iMEFs. To characterize the genomic regions where the three-dimensional genome structure was impaired in each condition, we divided the A and B compartment regions into five clusters mainly based on DNA and histone methylation status in 250 kb bins (Figure 3B, see Materials and Methods). ChIP-seq analysis showed higher lamin A/C enrichment in compartment B than in compartment A (Figure 3B), consistent with previous reports (39). DNA methylation levels in WT iMEFs were generally lower in the B compartments than in the A compartments, consistent with the frequent overlap of partially methylated DNA regions with the B compartments in differentiated cells (40). Although both B-1 and B-2 showed high H3K9me3 enrichment and lamin A/C association in the B compartments, other epigenetic, genomic, and 3D genome profiles were largely different between these clusters (Figure 3B). In particular, the density of L1 transposons and A/T content ratios were much higher in B-1 than in B-2 (the highest among all clusters); H3K9me2 and H3K27me3 in WT iMEFs were also higher in B-1 than in B-2, whereas

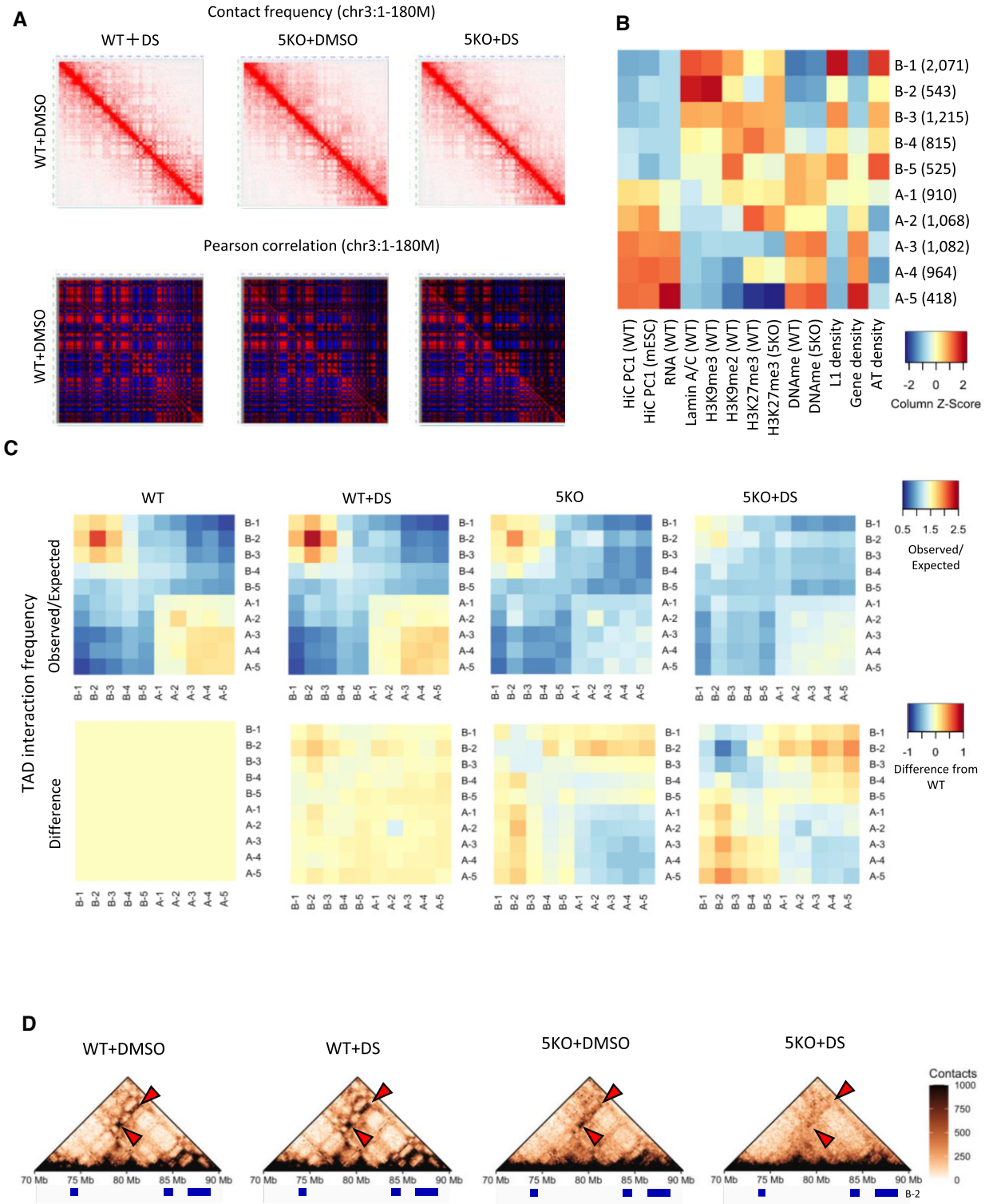

Figure 3. Impairment of heterochromatin-euchromatin segregation by the depletion of both H3K9 and H3K27 methylation. (**A**) Interaction matrix (top) and Pearson correlation matrix (bottom) of Hi-C data from WT and 5KO iMEFs treated with or without DS3201 along chromosome 3. Bin size is 500 kb. DS3201-treated 5KO iMEFs showed weakened compartmentalization between heterochromatin and euchromatin. (**B**) Heatmap of epigenetic and genetic features of each cluster. A and B compartments were further divided into five clusters mainly based on the HiC PC1 values (highest to lowest: A-5 > A-1 and B-5 > B-1) and other epigenetic and genetic features. The values for each feature were averaged for each cluster, then the averaged values were Z-scaled. The Z-scaled values are shown as the heatmap. (**C**) Heatmap of interaction between clusters. Each TAD was classified using cluster information in Figure 3B, then averaged Observed/Expected values of interaction frequency for each combination of TAD clusters are represented as a heatmap (top). The bottom heatmap shows the difference of the averaged Observed/Expected values from WT iMEFs (bottom). (**D**) Representative regions for B-2 TAD interaction. The pyramid plots represent interaction frequency within chr15: 70 000 000–90 000 000. Red arrow heads represent B-2-to-B-2 interaction and blue boxes represent B-2 TADs.

Hi-C PC1 values in mESCs (16) were higher in B-2 than in B-1 (Figure 3B, Supplementary Figure S7b). Notably, 4.0% and 27.3% of B-1 and B-2 were the A compartments in mESCs, respectively, which suggests that B-2 tends to be a cell type-specific B compartment.

Next, we characterized the chromatin interactions between clusters. Since chromatin interacts on a topologically associating domain (TAD)-by-TAD basis, we identified the TAD boundary in WT iMEFs and classified TAD using the cluster information shown in Figure 3B (Supplementary Figure S7c, d). More than 100 TADs were identified for each type (Supplementary Figure S7e). The heatmap of the interaction frequency between TAD types shows that the A compartments were segregated from the B compartments in WT iMEFs. The segregation was weakened in 5KO iMEFs and DS3201-treated 5KO iMEFs (Figure 3C). B-2 TADs interacted strongly with each other and moderately with B-1 and B-3 TADs, all of which showed higher H3K9me3 enrichment than B-4 and B-5 (Figure 3B, C). The interaction of B compartment clusters with B-2 decreased in 5KO iMEFs and further decreased in DS3201-treated 5KO iMEFs (Figure 3C, D). As H3K27me3 was acquired in the B-2 TADs after the loss of H3K9 methylation (Figure 3B, Supplementary Figure S7f), it is assumed that H3K27me3 redistribution maintains the B-2 TAD-related interactions after the loss of H3K9 methylation. In the B compartments, decreased inter-TAD interactions in 5KO iMEFs were mainly observed in B-2 TADs, and the interactions among other clusters, such as inter B-3 TADs and inter B-4 TADs, were also decreased in DS3201-treated 5KO iMEFs (Figure 3C). Thus, the global impairment of heterochromatin interactions is caused by the depletion of H3K9 and H3K27 methylation.

Although the interactions between TADs were significantly altered in DS3201-treated 5KO iMEFs, there were no noticeable changes in the genomic distribution of TAD boundaries, as indicated by the similarity in the distribution of insulation scores along chromosomes across samples (Supplementary Figure S8a). However, the insulation score at the TAD boundary was found to have increased in 5KO iMEFs (Supplementary Figure S8b), suggesting that insulation at the TAD boundary was weakened in 5KO cells. We observed decreased interaction frequency within TADs in 5KO iMEFs (Supplementary Figure S8c, d), particularly evident in the interactions between TAD boundaries (Supplementary Figure S8d). Notably, further weakened insulation and decreased intra-TAD interactions were not observed after treatment with DS3201 in 5KO iMEFs (Supplementary Figure S8b, d). Thus, intra-TAD interactions and insulation were impaired in 5KO iMEFs regardless of H3K27me3 redistribution.

Epigenetic and genetic features of compartment conversion and lamin A/C dissociation induced by the depletion of H3K9 and H3K27 methylation

Next, we investigated the impairment of 3D genome organization after the depletion of H3K9 and H3K27 methylation from the viewpoint of the nuclear compartment and localization in the nuclear periphery using Hi-C PC1 values and lamin A/C enrichments in 250 kb bins. DS3201-treated 5 KO iMEFs exhibited the most significant impairment in Hi-C PC1 values and lamin A/C enrichment (Supplementary Figure S9a). Despite the negative correlation between the changes in Hi-C PC1 values and lamin A/C enrichment caused by DS3201 treatment in 5KO iMEFs (Supplementary Figure S9b), lamin A/C enrichment was more severe impairment than Hi-C PC1 values in DS3201-treated 5KO iMEFs (Supplementary Figure S9a). We observed it increased Hi-C PC1 values and decreased lamin A/C enrichment in the B-2 cluster of 5KO iMEFs (Figure 4A, B), while DS3201-treated 5KO iMEFs showed increased Hi-C PC1 and decreased lamin A/C enrichment also in the B-3 and B-4 clusters (Figure 4A, B). We also observed the overall maintenance of both Hi-C PC1 values and lamin A/C enrichment in the B-1 cluster, even in DS3201-treated 5KO iMEFs (Figure 4A, B), indicating that epigenetic pathways other than H3K9 and H3K27 methylation complemented or functioned in parallel with these pathways.

The impairment of Hi-C PC1 values resulted in weakened compartment formation and compartment conversion (Figure 4C), and B-to-A conversion was correlated with lamin A/C dissociation (Figure 4C). Among the 5169 250 kb bins in the B compartments in WT iMEFs, 219, 453 and 760 250 kb bins showed B-to-A conversion in DS3201-treated WT iMEFs, 5KO iMEFs, and DS3201-treated 5KO iMEFs, respectively. We also identified a 250 kb bin where lamin A/C was converted from enriched ($\log_2$(ChIP/Input $>$ 0)) in WT iMEFs to non-enriched ($\log_2$(ChIP/Input $<$ 0)) in each sample. Among the 4277 lamins A/C-enriched 250 kb bins in WT iMEFs, 261, 644 and 1256 250 kb bins showed a loss of lamin A/C enrichment in DS3201-treated WT iMEFs, 5KO iMEFs, and DS3201-treated 5KO iMEFs, respectively. Even when we analyzed the frequencies of B-to-A conversion and lamin A/C dissociation for each cluster, the frequencies of B-to-A conversion and lamin A/C dissociation in all B-compartment clusters, except for the B-5 cluster, were the highest in DS3201-treated 5KO iMEFs (Supplementary Figure S9c). We noticed that the frequency of lamin A/C dissociation was approximately six times higher than the frequency of B-to-A conversion in the B-1 cluster in DS3201-treated 5KO iMEFs (Supplementary Figure S9c). Thus, B-1 clusters are resistant to compartment conversion, but a subset of B-1 clusters can be detached from the nuclear periphery without compartment conversion after depletion of both H3K9 and H3K27 methylation.

Next, we investigated the differences between B-to-A-switched regions and lamin A/C-dissociated regions. Consistent with the B-1 cluster being characterized by low Hi-C PC1 values in mESCs and high L1 density (Figure 3B), B-to-B unswitched regions were less frequently associated with iMEF-specific B compartments (Supplementary Figure S9d) and had higher L1 density (Supplementary Figure S9e, upper panels) than B-to-A-switched regions. Although L1 density was significantly higher in lamin A/C-maintained regions than in lamin A/C-dissociated regions in DS3201-treated 5KO iMEFs (Supplementary Figure S9e), the lamin A/C-dissociated regions were frequently located in high L1 density regions (top 25% of L1 density) at a frequency similar to that observed in the B-to-B unswitched regions (B-to-B:48.4%, B-to-A:14.7%, lamin

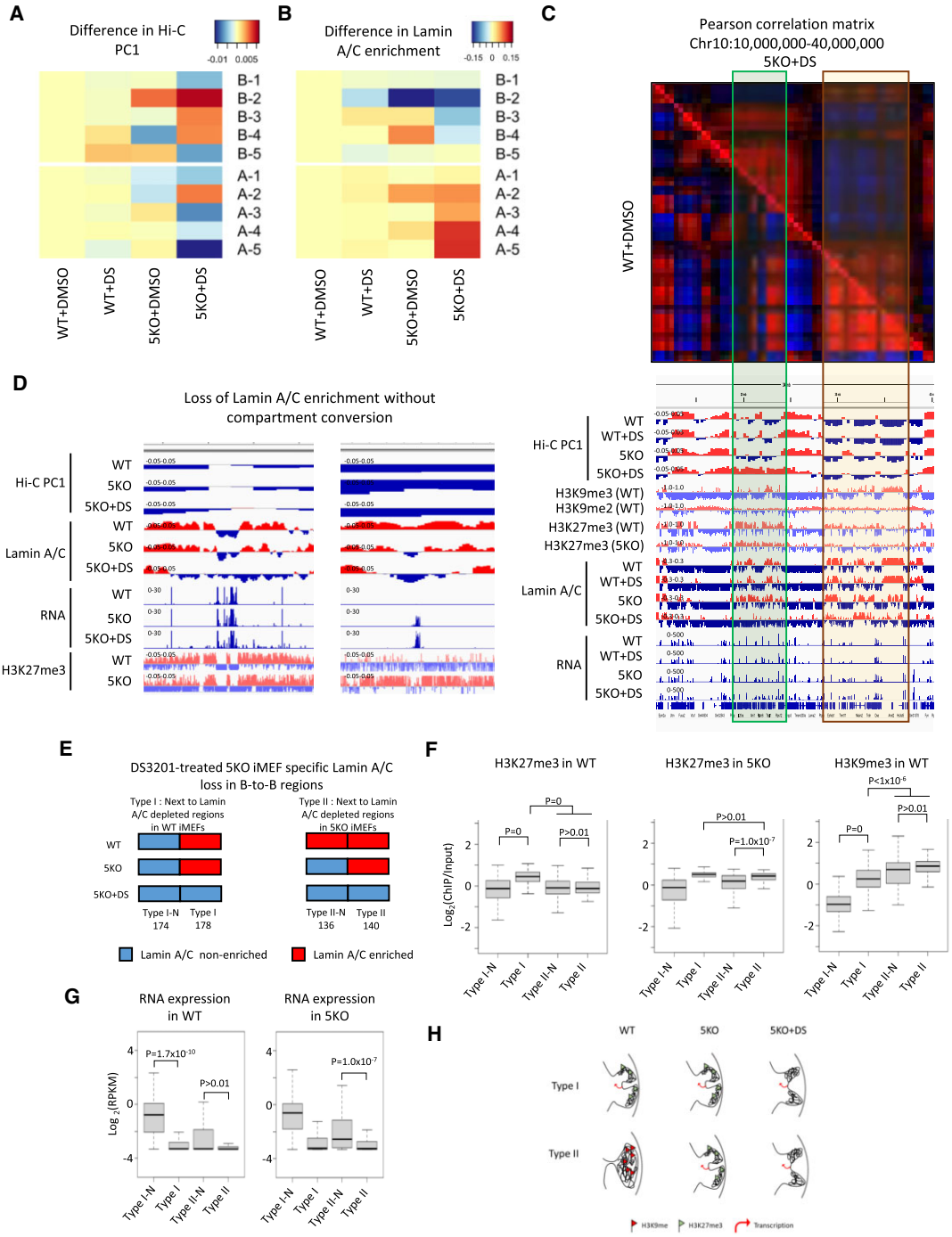

Figure 4. Features of B-to-A compartment conversion and lamin A/C dissociation in H3K9 and H3K27 methylation depleted cells. (A, B) Heatmaps of difference in Hi-C PC1 values (**A**) or difference in lamin A/C enrichment (**B**) in each sample. The difference of Hi-C PC1 values or lamin A/C enrichment between samples were calculated in each 250 kb bin, then these values were averaged for each cluster. (**C**) Representative view of B-to-A changes in DS3201-treated 5KO iMEFs in chr10:10 000 000–40 000 000. The upper figure represents Pearson correlation matrix of Hi-C data from WT and DS3201-treated 5KO iMEFs, and the bottom figure represents Hi-C PC1 values and epigenetic profiles in this genomic region. Genomic regions surrounded by green and orange boxes represent B-to-A switched and B-to-B unswitched regions, respectively, in DS3201-treated 5KO iMEFs, respectively. (**D**) Representative lamin A/C dissociated regions without compartment conversion in DS3201-treated 5KO iMEFs. (**E**) Two types of the DS3201-treated 5KO iMEFs specific lamin A/C dissociated regions (named 5DSLs) in the B-to-B unswitched group. Type I region, Type I was adjacent to a region (named as Type I-N) at which lamin A/C association was absent in WT and 5KO (±DS3201) iMEFs. Type II region, Type II was adjacent to a region (Type II-N) at which lamin A/C was associated in WT but lost in 5KO (±DS3201) iMEFs. The number shown in the bottom represents the number of each analyzed regions. (**F**) Box plots of H3K27me3 enrichment in WT iMEFs (left) or 5KO iMEFs (center), and H3K9me3 enrichment in 5KO iMEFs (right). (**G**) Box plots of RNA expression levels of WT (left) and 5KO (right) iMEFs in each region. RNA expression levels were calculated as $\log_2$(RPKM) in each 250 kb bin. (**H**) Summary of epigenome and lamin A/C dissociation profiles in Type I and Type II regions. In the box plots shown in Figure 4, the medians are shown by center lines. Box limits indicate the 25th and 75th percentiles and whiskers extend 1.5 times the interquartile range from the 25th and 75th percentiles. *P* values by Tukey's test (unpaired, two-tailed) are indicated.

A/C dissociated:41.0%, lamin A/C maintained:49.9%). We also observed B-to-A switched regions near the A compartments in WT iMEFs, compared to the lamin A/C dissociated regions without compartment conversion in DS3201-treated 5KO iMEFs (Supplementary Figure S9f). Thus, genomic regions characterized by low L1 density and located near the A compartments tended to show compartment conversion. In contrast, high L1 density and located far from the A compartments were more dissociated from the nuclear membrane without compartment conversion in DS3201-treated 5KO iMEFs. Regardless of the different features of lamin A/C dissociation and compartment conversion, both were associated with increased RNA expression (Supplementary Figure S9g).

We also found that lamin A/C dissociation, observed explicitly in DS3201-treated 5KO iMEFs without compartment conversion, frequently occurred near detached lamin A/C regions in WT and 5KO iMEFs (Figure 4D, Supplementary Figure S9h). To further investigate this finding in detail, the DS3201-treated 5KO iMEF-specific lamin A/C dissociated regions were classified into two types; one (named Type I) was adjacent to a region (named Type I-N) at which the lamin A/C association was absent in WT and 5KO (±DS3201) iMEFs, while the other type, Type II, was adjacent to a region (Type II-N) at which lamin A/C was associated in WT, but was lost in 5KO (±DS3201) iMEFs (Figure 4E). Histone modification profiles in each region showed that H3K27me3 in WT iMEFs was enriched only in Type I regions, whereas Type II regions acquired H3K27me3 in 5KO iMEFs (Figure 4F). In contrast, H3K9me3 was absent in WT iMEFs only in type I-adjacent regions (Type I-Ns) (Figure 4F). Transcription profiles of each region showed that Type I-Ns were highly transcribed in WT iMEFs but not in other regions (Figure 4G), whereas Type II-Ns were transcriptionally activated in 5KO iMEFs (Figure 4G). These data suggest that H3K27me3 prevents the expansion of lamin A/C dissociation caused by the activation of neighboring transcriptions (Figure 4H).

We also performed ChIP-seq analysis of lamin B1, a distinct nuclear lamina protein, and revealed that its distribution resembled that of lamin A/C in all samples, indicating considerable disruption of its interaction with the nuclear envelope due to the loss of H3K9/K27 methylation (Supplementary Figure S10). In addition, redistribution of H3K27me3 and impairment of the spatial organization of heterochromatin were consistently observed in another 5KO clone, clone 14 (Supplementary Figure S11).

H3K27me3 regulates the spatial organization of heterochromatin independently of H2AK119 monoubiquitylation (H2Aub)

Finally, we investigated the role of H2Aub, another polycomb-mediated repressive chromatin modification, in heterochromatin organization after the loss of H3K9 methylation. H2Aub is mediated by the E3 ubiquitin ligases RING1A and RING1B, which are components of the polycomb group (PcG) complex 1 (PRC1). H2Aub may be involved in heterochromatin organization after the loss of H3K9 methylation because it has been reported that H2Aub is also redistributed to the chromocenter after the loss of H3K9me3 (41,42). Consistent with this report, catch-seq analysis of H2Aub in WT and 5KO iMEFs showed that H2Aub was redistributed to the B compartment in 5KO iMEFs (Figure 5A). We established 5KO + *Ring1b* KO cell lines by further inactivating *Ring1b* based on 5KO #55 using the CRISPR-Cas9 system to investigate the function of H2Aub in heterochromatin organization after the loss of H3K9 methylation (Supplementary Figure S12a–c). Further knockdown of *Ring1a* by shRNA in 5KO-*Ring1b* KO cells efficiently reduced H2Aub modification (Supplementary Figure S12d, e). *in situ* Hi-C analysis of 5KO + *Ring1b* KO cells with depletion of Ring1A showed different features of the Hi-C PC1 pattern from DS3201-treated 5KO iMEFs (Figure 5B) and maintained TAD–TAD interactions in the B compartments (Figure 5C). These results suggest that H3K27me3 maintains the spatial organization of heterochromatin, independent of H2Aub. As mentioned, almost all B compartments were maintained in the DS3201-treated 5KO iMEFs. Since H2Aub remained in the H3K9me2/3-marked B compartments of DS3201-treated 5KO iMEFs (Figure 5A), this modification may contribute to maintaining B compartments after the loss of H3K9 and H3K27 methylation.

DISCUSSION

Herein, we report the impact of H3K9 and H3K27 methylation on heterochromatin organization by assessing genetic and pharmacological perturbations of histone methyltransferases in iMEFs. This is the first report of a global 3D genome and heterochromatin organization analysis in mammalian cells depleted of two repressive chromatin modifications, namely H3K9me2/3 and H3K27me3. We showed that both H3K9 and H3K27 methylation pathways are critical for structural and spatial heterochromatin organization, including chromocenter formation, heterochromatin-euchromatin segregation, association with NL, and compartment formation. The H3K9 and H3K27 methylation pathways are required to form B compartments, especially L1-poor facultative heterochromatin located near the A/B compartment boundaries (Figure 6). Although the impairment of heterochromatin, characterized by the partial loss of small electron-dense materials as observed during EM analysis, was already observed in 5KO iMEFs (Figure 2C), 6KO iMEFs established in Thomas Jenuwein's lab showed more severe heterochromatin impairment than our 5KO iMEFs (15). There were two major differences between the 6KO and 5KO cases. The first difference is that their 6 KO iMEFs lacked *Setdb2* in addition to the five methyltransferases missing from our 5 KO iMEFs. SETDB2 might have a role in heterochromatin maintenance in our 5KO iMEFs, inactivation of *Setdb2* was not required for the complete depletion of H3K9 methylation in our case. The second difference was that 6KO iMEFs used 4-hydroxytamoxifen (4OHT)-inducible conditional *Setdb1* KO in *Suv39h1*/*Suv39h2*/*Ehmt1*/*Ehmt2*/*Setdb2* KO iMEFs, and the heterochromatin states 4 days after the treatment of 4OHT. Although an increase in H3K27me3 was also observed in their 6KO iMEFs (15), the compensation of heterochromatin maintenance by PRC2-mediated H3K27 methylation after the complete loss of H3K9 methy-

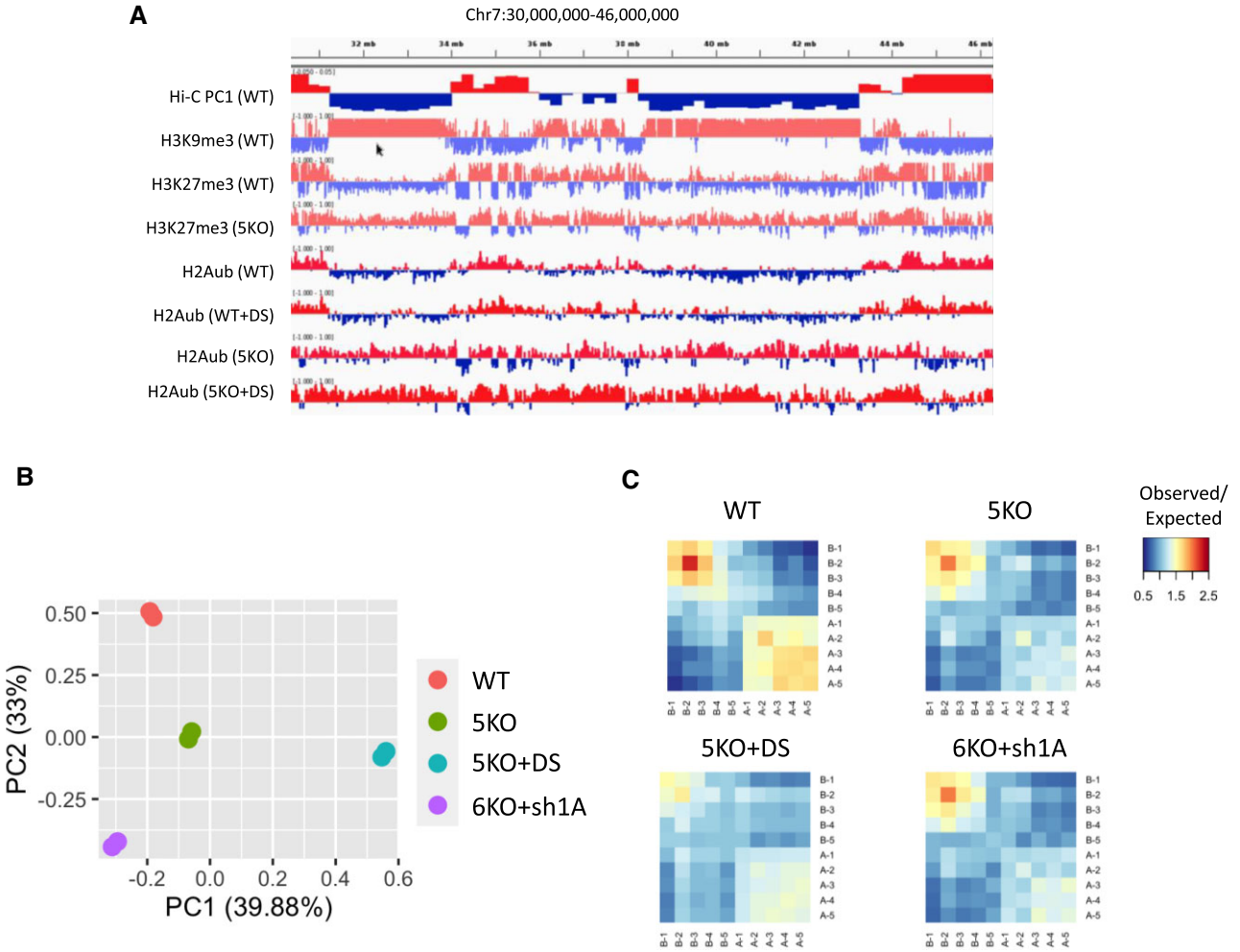

Figure 5. Functional independence of H3K27me3 and H2Aub in heterochromatin regulation. (**A**) Genomic distribution of H2Aub in WT, 5KO and DS3201-treated 5KO iMEFs. (**B**) PCA plots of Hi-C PC1 values of 250-kb bin in WT, 5KO, DS3201-treated 5KO, and 5KO-*Ring1b* KO + sh*Ring1a* iMEFs. (**C**) Heatmap of interaction between clusters. Each TAD was classified using cluster information in Figure 3B, then averaged Observed/Expected values of interaction frequency for each combination of TAD clusters were represented as a heatmap.

lation four days after 4OHT treatment might be less efficient than that in our established 5KO iMEFs. These differences may underlie the differences in heterochromatin states between the 6KO and 5KO iMEFs.

We found that H3K27me3 was redistributed into the B compartments after the loss of H3K9 methylation. Our EM analysis revealed that the DS3201 treatment of 5KO iMEFs significantly decreased the number of electron-dense regions. While the histone modification status of these regions remained unclear by EM analysis, the fact that electron-dense regions did not decrease and increased in WT treated with DS3201 suggests that H3K27me3 does not significantly contribute to the electron-dense formation in WT iMEFs, but its redistribution in 5KO iMEFs contributes significantly to the formation of electron-dense regions. However, even in this case, it is unclear how H3K27me3 can compensate for the chromatin condensation function mediated by H3K9 methylation after depletion of H3K9 methylation. If the B-4 region is the main H3K27me3-marked facultative B heterochromatin, B-4 is more L1-poor/GC-rich and gene-rich than the B-1 and B-2 subregions. In the B-4 regions, H3K27me3 is insufficient for chromatin condensation, but H3K27me3 may replace the chromatin condensation function of H3K9me2/3 in the B-1 and B-2 regions.

The redistribution of H3K27me3 linked to the depletion of H3K9me3 has been reported in both *Neurospora crassa* and mammals (17,18,43). In mice, constitutive heterochromatin formed by pericentromeric satellite repeats (PCH) is rich in H3K9me3, mediated by SUV39H1/2 and devoid of H3K27me3. *Suv39h1/2* DKO mouse cells exhibit a loss of H3K9me3 in the PCH, accompanied by reduced DNA methylation and a gain of H3K27me3 in the PCH (44). The redistribution of H3K27me3 to PCH is also induced by DNA hypomethylation, and BEND3, a DNA methylation-sensitive DNA-binding protein, is necessary for the PRC2 recruitment to hypomethylated PCH (44). Redistribution of H3K27me3 to H3K9me3-target regions in hypomethylated DNA states has also been observed in other physiological conditions, such as early mouse embryo and germ cell development (42,45,46) and during cellular senescence (47). In our 5KO iMEFs, DNA methylation decreased, especially in the B compartments, but not

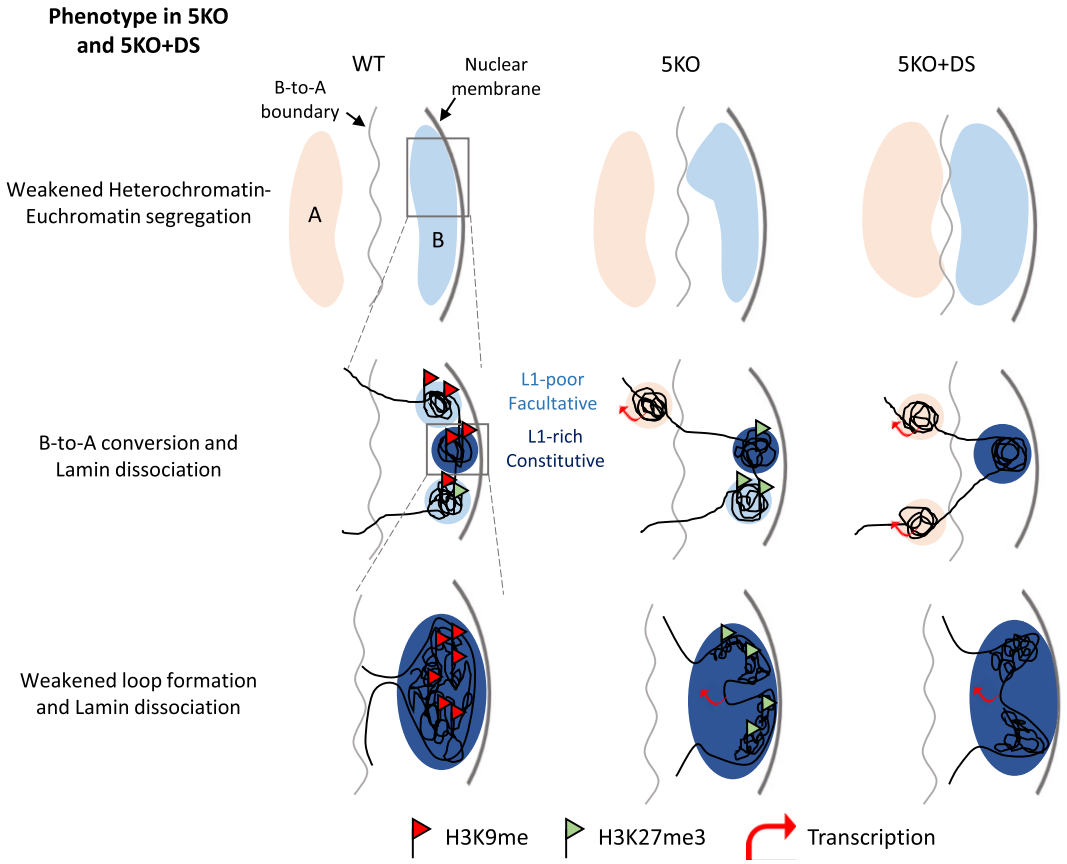

Figure 6. Summary of epigenome and 3D genome changes in H3K9/K27 methylation deficient cells. (Top) Degree of heterochromatin-euchromatin segregation was maintained after the loss of H3K9 methylation, but was significantly weakened in DS3201-treated 5KO iMEFs. (Middle) B-to-A compartment conversions in 5KO and DS3201-treated 5KO iMEFs were frequently occurred in the B compartments near A/B compartment boundary. Such regions had both H3K9me and H3K27me3 in WT iMEFs and L1 poor and the compartment conversion was frequently associated with lamin A/C dissociation and transcriptional activation. (Bottom) In 5KO iMEFs, interaction frequency at loops was decreased, suggesting regulation of loop formation by H3K9me. In addition, transcriptional activation associated lamin A/C dissociation was observed in internal of the B compartments in 5KO iMEFs, which was not accompanied by compartment conversion. H3K27me3 was enriched around lamin A/C dissociated regions in 5KO iMEFs and the dissociated regions were expanded in DS3201-treated 5KO iMEFs.

in transcriptionally active regions. In mouse oocytes, DNA methylation in transcriptionally active regions is retained by SETD2-mediated H3K36me3, and *Setd2*-deficient oocytes show H3K27me3 invasion into the gene body (48). Thus, DNA methylation may restrict the spread of H3K27me3 in both active and inactive regions. In addition to DNA methylation, H3K27me3 invasion was less effective in the B compartments far from the A/B compartment boundaries in 5KO iMEFs (Figure 1C). As H3K27me3 tended to be enriched in the A/B compartment boundaries in WT iMEFs, H3K27me3 invasion may have been induced mainly by spreading from the existing H3K27me3 regions in 5KO iMEFs.

We also revealed the strengthening of heterochromatin, as indicated by an increase in the number of chromocenters (Supplementary Figure S4b), the volume of chromocenters (Supplementary Figure S4c), electron-dense regions under the electron microscope (Figure 2C), and B-2-related interactions (Figure 3C), through DS3201 treatment in WT iMEFs. A recent study conducted by Aryee and Liau examining the impact of H3K27me3 loss (treatment with GSK343, another EZH2 inhibitor) on 3D genome organization found that H3K9me3 spreads to Polycomb-targeted B regions (H3K27me3-marked PcG-B regions) following H3K27me3 loss, resulting in lamina repositioning and strengthening of the B compartments; therefore, genes in the PcG-B regions are not derepressed (49). Thus, similar to H3K27 methylation, H3K9 methylation also responds to H3K27 methylation loss and compensates for H3K27 function in heterochromatin configuration.

We found that the H3K9 or H3K27 methylation pathway is sufficient for heterochromatin condensation and maintaining long-range interactions, but how? HP1 binds to methylated H3K9 (highest to H3K9me3) and condenses chromatin (9–13). HP1 depletion in *Drosophila* embryos results in weakened compartmentalization of the B compartments (14). H3K27me3 is recognized by a chromodomain protein in the canonical PRC1 (50–52), which mediates H2AK119 monoubiquitylation and chromatin compaction (53–55). Since PRC1 also regulates long-range (>10 Mb) promoter interactions (56), PRC1 may function downstream of H3K27me3 in heterochromatin organization after the loss of H3K9 methylation. However, our analysis of 5KO-Ring1A/B-depleted cells showed that at

least H2Aub was not required for H3K27me3-mediated heterochromatin-euchromatin organization. Since structural maintenance of the chromosome hinge domain containing 1 (Smchd1) is a noncanonical SMC protein that regulates chromatin compaction and long-range interactions of H3K27me3-marked genomic regions, such as the inactive X chromosome and *Hox* gene cluster (57–60), Smchd1 and other components of PRC1 besides Ring1A/Ring1B may control H3K27me3-dependent heterochromatin organization redundantly or independently.

Although heterochromatin-euchromatin segregation is globally impaired in iMEFs depleted of both H3K9 methylation and H3K27me3, L1-rich, A/T-rich, and gene-poor B-1 regions of the B compartment are largely maintained, indicating the presence of H3K9 and H3K27 methylation pathway-independent mechanism(s) for B compartment formation; PRC1 (56), RNAs (61,62), histone acetylation (63), replication timing (RT) (8) and the nuclear lamina (39,64) may be involved. Concerning RT control, the master regulator of RT, RIF1, is mainly enriched in late-replicating H3K9me3-riched B compartment regions (8,65) and B compartment regions showing RT switch resistance to RIF1 depletion are partially induced to a late-to-early replication switch when H3K9me3 is depleted (8,65), suggesting that H3K9/K27 methylation and RIF1 may contribute redundantly to the heterochromatinization of B-1 regions, which may be maintained if either one is functional. Furthermore, as active chromatin modifications, such as H3K27ac, remain depleted even after the loss of H3K9/K27 methylation in the B compartments (data not shown), the HDAC pathway may maintain the B compartments after the loss of H3K9/K27 methylation. The characteristics of the B-1 region are a feature of cell type-independent constitutive LADs (cLADs) (66), and the present findings help understand the formation of cLADs. Various factors have been speculated to be involved in forming nuclear compartments. It is expected that all forms of H3K9 methylation and H3K27me3 depleted cells established in this study will be valuable resources for investigating the entire mechanism of nuclear compartmentalization. Our study provides evidence for the redundant regulation of heterochromatin organization mediated by H3K9 and H3K27 methylation pathways.

DATA AVAILABILITY

All reads from the WGBS, RNA-seq, Histone ChIP-seq, Lamin A/C and B1 ChIP-seq, and Hi-C experiments generated in this study have been submitted to the Gene Expression Omnibus under the accession numbers GSE200010, GSE200015, GSE200011, GSE200014, GSE200016 and GSE200012, respectively.

SUPPLEMENTARY DATA

Supplementary Data are available at NAR Online.

ACKNOWLEDGEMENTS

We thank the staff of the Support Unit for Bio-Material Analysis (BMA) at the RIKEN Center for Brain Science (CBS) Research Resources Division (RRD) for NGS library construction, DNA sequencing and flow cytometry, and Yosky Kataoka at RIKEN BDR for the support of EM analysis. This study used the following materials: pL-CRISPR.EFS.tRFP from Benjamin Ebert, pKLV2-U6gRNA5(Bbsl)-PGKpuro2ABFP from Kosuke Yusa, polyclonal antibody against lamin A (323–10) from Robert D. Goldman, and monoclonal antibody against Ring1B from Haruhiko Koseki. We would also like to thank Tatsuya Hirano for his valuable comments on this study, our colleagues at Shinkai laboratory for their support and valuable comments.

Author contributions: K.F. and Y.S. designed and conceived the study. K.F., H.K. and Y.S. supervised the study. K.F., T. Shimi, H.K. and Y.S. interpreted the data. K.F., T. Shimi, A.I. and C.S. performed molecular, cellular and fluorescence microscopic experiments and generated the ChIP-seq, RNA-seq and Hi-C-seq libraries. C.S. generated KO iMEF cell lines with the help from K.F. and Y.S. T.O. performed chromatin microscopic analysis of the KO iMEF lines. T. Suzuki and N.D. performed MS analysis of H3K9 and H3K27 methylation for the established KO iMEF lines. K.O., S.O. and S.Y. performed EM analysis of the established KO iMEF nucleus. H.M. and I.H. performed and consulted for informatics analysis of Hi-C-seq data. K.I. and Y.O. designed the TALE probe for major satellite repeats. K.F. and Y.S. wrote the manuscript and prepared figures. All authors read, discussed, and approved the manuscript.

FUNDING

RIKEN internal research fund (Pioneering project 'Genome building from TADs') (to Y.S.); Special Postdoctoral Researcher (SPDR) Program of RIKEN (to K.F.); Y.S. was also supported by the Japan Society for the Promotion of Science (JSPS) [for Grant-in-Aid for Scientific Research [A], JP18H03991 and JP22H00413; Grant-in-Aid for Scientific Research on Innovative Areas (Research in a proposed research area), JP18H05530]; H.K. was supported by the JSPS [for Grant-in-Aid for Scientific Research [A], JP21H04764; and for a Grant-in-Aid for Scientific Research on Innovative Areas (Research in a proposed research area), JP18H05527]; S.Y. was supported by JSPS [for Grant-in-Aid for Scientific Research [B], JP18H02617]; Japan Science and Technology (JST) [for Moonshot R&D, JPMJMS2022]; T. Shimi was supported by JSPS [for Grant-in-Aid for Scientific Research [C], JP20K06617]. Funding for open access charge: Japan Society for the Promotion of Science.

Conflict of interest statement. None declared.

REFERENCES

1. Allshire,R.C. and Madhani,H.D. (2018) Ten principles of heterochromatin formation and function. *Nat. Rev. Mol. Cell Biol.*, **19**, 229–244.
2. Lieberman-Aiden,E., van Berkum,N.L., Williams,L., Imakaev,M., Ragoczy,T., Telling,A., Amit,I., Lajoie,B.R., Sabo,P.J., Dorschner,M.O *et al.* (2009) Comprehensive mapping of long-range interactions reveals folding principles of the human genome. *Science*, **326**, 289–293.

3. van Steensel,B. and Belmont,A.S. (2017) Lamina-associated domains: links with chromosome architecture, heterochromatin, and gene repression. *Cell*, **169**, 780–791.
4. Kind,J., Pagie,L., de Vries,S.S., Nahidiazar,L., Dey,S.S., Bienko,M., Zhan,Y., Lajoie,B., de Graaf,C.A., Amendola,M. *et al.* (2015) Genome-wide maps of nuclear lamina interactions in single human cells. *Cell*, **163**, 134–147.
5. Madsen-Osterbye,J., Bellanger,A., Galigniana,N.M. and Collas,P. (2022) Biology and model predictions of the dynamics and heterogeneity of chromatin-nuclear lamina interactions. *Front. Cell Dev. Biol.*, **10**, 913458.
6. Wen,B., Wu,H., Shinkai,Y., Irizarry,R.A. and Feinberg,A.P. (2009) Large histone H3 lysine 9 dimethylated chromatin blocks distinguish differentiated from embryonic stem cells. *Nat. Genet.*, **41**, 246–250.
7. Falk,M., Feodorova,Y., Naumova,N., Imakaev,M., Lajoie,B.R., Leonhardt,H., Joffe,B., Dekker,J., Fudenberg,G., Solovei,I. *et al.* (2019) Heterochromatin drives compartmentalization of inverted and conventional nuclei. *Nature*, **570**, 395–399.
8. Klein,K.N., Zhao,P.A., Lyu,X., Sasaki,T., Bartlett,D.A., Singh,A.M., Tasan,I., Zhang,M., Watts,L.P., Hiraga,S.I. *et al.* (2021) Replication timing maintains the global epigenetic state in human cells. *Science*, **372**, 371–378.
9. Hiragami-Hamada,K., Soeroes,S., Nikolov,M., Wilkins,B., Kreuz,S., Chen,C., De La Rosa-Velazquez,I.A., Zenn,H.M., Kost,N., Pohl,W. *et al.* (2016) Dynamic and flexible H3K9me3 bridging via HP1beta dimerization establishes a plastic state of condensed chromatin. *Nat. Commun.*, **7**, 11310.
10. Bannister,A.J., Zegerman,P., Partridge,J.F., Miska,E.A., Thomas,J.O., Allshire,R.C. and Kouzarides,T. (2001) Selective recognition of methylated lysine 9 on histone H3 by the HP1 chromo domain. *Nature*, **410**, 120–124.
11. Lachner,M., O'Carroll,D., Rea,S., Mechtler,K. and Jenuwein,T. (2001) Methylation of histone H3 lysine 9 creates a binding site for HP1 proteins. *Nature*, **410**, 116–120.
12. Azzaz,A.M., Vitalini,M.W., Thomas,A.S., Price,J.P., Blacketer,M.J., Cryderman,D.E., Zirbel,L.N., Woodcock,C.L., Elcock,A.H., Wallrath,L.L. *et al.* (2014) Human heterochromatin protein 1alpha promotes nucleosome associations that drive chromatin condensation. *J. Biol. Chem.*, **289**, 6850–6861.
13. Zeng,W., Ball,A.R. and Yokomori,K. (2010) HP1: heterochromatin binding proteins working the genome. *Epigenetics*, **5**, 287–292.
14. Zenk,F., Zhan,Y., Kos,P., Loser,E., Atinbayeva,N., Schachtle,M., Tiana,G., Giorgetti,L. and Iovino,N. (2021) HP1 drives de novo 3D genome reorganization in early Drosophila embryos. *Nature*, **593**, 289–293.
15. Montavon,T., Shukeir,N., Erikson,G., Engist,B., Onishi-Seebacher,M., Ryan,D., Musa,Y., Mittler,G., Meyer,A.G., Genoud,C. *et al.* (2021) Complete loss of H3K9 methylation dissolves mouse heterochromatin organization. *Nat. Commun.*, **12**, 4359.
16. Fukuda,K., Shimura,C., Miura,H., Tanigawa,A., Suzuki,T., Dohmae,N., Hiratani,I. and Shinkai,Y. (2021) Regulation of mammalian 3D genome organization and histone H3K9 dimethylation by H3K9 methyltransferases. *Commun. Biol.*, **4**, 571.
17. Peters,A.H., Kubicek,S., Mechtler,K., O'Sullivan,R.J., Derijck,A.A., Perez-Burgos,L., Kohlmaier,A., Opravil,S., Tachibana,M., Shinkai,Y. *et al.* (2003) Partitioning and plasticity of repressive histone methylation states in mammalian chromatin. *Mol. Cell*, **12**, 1577–1589.
18. McCarthy,R.L., Kaeding,K.E., Keller,S.H., Zhong,Y., Xu,L., Hsieh,A., Hou,Y., Donahue,G., Becker,J.S., Alberto,O. *et al.* (2021) Diverse heterochromatin-associated proteins repress distinct classes of genes and repetitive elements. *Nat. Cell Biol.*, **23**, 905–914.
19. Dubos,T., Poulet,A., Thomson,G., Pery,E., Chausse,F., Tatout,C., Desset,S., van Wolfswinkel,J.C. and Jacob,Y. (2022) NODeJ: an ImageJ plugin for 3D segmentation of nuclear objects. *BMC Bioinformatics*, **23**, 216.
20. Anton,T., Bultmann,S., Leonhardt,H. and Markaki,Y. (2014) Visualization of specific DNA sequences in living mouse embryonic stem cells with a programmable fluorescent CRISPR/cas system. *Nucleus*, **5**, 163–172.
21. Ikeda,T., Hikichi,T., Miura,H., Shibata,H., Mitsunaga,K., Yamada,Y., Woltjen,K., Miyamoto,K., Hiratani,I., Yamada,Y *et al.* (2018) Srf destabilizes cellular identity by suppressing cell-type-specific gene expression programs. *Nat. Commun.*, **9**, 1387.
22. Kadota,M., Nishimura,O., Miura,H., Tanaka,K., Hiratani,I. and Kuraku,S. (2020) Multifaceted Hi-C benchmarking: what makes a difference in chromosome-scale genome scaffolding?. *Gigascience*, **9**, giz158.
23. Durand,N.C., Shamim,M.S., Machol,I., Rao,S.S., Huntley,M.H., Lander,E.S. and Aiden,E.L. (2016) Juicer provides a one-click system for analyzing loop-resolution hi-C experiments. *Cell Syst.*, **3**, 95–98.
24. Miura,H., Poonperm,R., Takahashi,S. and Hiratani,I. (2018) Practical analysis of Hi-C data: generating A/B compartment profiles. *Methods Mol. Biol.*, **1861**, 221–245.
25. Miura,H., Takahashi,S., Poonperm,R., Tanigawa,A., Takebayashi,S.I. and Hiratani,I. (2019) Single-cell DNA replication profiling identifies spatiotemporal developmental dynamics of chromosome organization. *Nat. Genet.*, **51**, 1356–1368.
26. Rowley,M.J., Poulet,A., Nichols,M.H., Bixler,B.J., Sanborn,A.L., Brouhard,E.A., Hermetz,K., Linsenbaum,H., Csankovszki,G., Lieberman Aiden,E. *et al.* (2020) Analysis of hi-C data using SIP effectively identifies loops in organisms from *C. elegans* to mammals. *Genome Res.*, **30**, 447–458.
27. van der Weide,R.H., van den Brand,T., Haarhuis,J.H.I., Teunissen,H., Rowland,B.D. and de Wit,E. (2021) Hi-C analyses with GENOVA: a case study with cohesin variants. *NAR Genom Bioinform*, **3**, lqab040.
28. Langmead,B., Trapnell,C., Pop,M. and Salzberg,S.L. (2009) Ultrafast and memory-efficient alignment of short DNA sequences to the human genome. *Genome Biol.*, **10**, R25.
29. 1000 Genome Project Data Processing Subgroup, Li,H., Handsaker,B., Wysoker,A., Fennell,T., Ruan,J., Homer,N., Marth,G., Abecasis,G. and Durbin,R. (2009) The sequence alignment/map format and samtools. *Bioinformatics*, **25**, 2078–2079.
30. Liao,Y., Smyth,G.K. and Shi,W. (2014) featureCounts: an efficient general purpose program for assigning sequence reads to genomic features. *Bioinformatics*, **30**, 923–930.
31. Trapnell,C., Pachter,L. and Salzberg,S.L. (2009) TopHat: discovering splice junctions with RNA-seq. *Bioinformatics*, **25**, 1105–1111.
32. Jin,Y., Tam,O.H., Paniagua,E. and Hammell,M. (2015) TEtranscripts: a package for including transposable elements in differential expression analysis of RNA-seq datasets. *Bioinformatics*, **31**, 3593–3599.
33. Love,M.I., Huber,W. and Anders,S. (2014) Moderated estimation of fold change and dispersion for RNA-seq data with DESeq2. *Genome Biol.*, **15**, 550.
34. Krueger,F. and Andrews,S.R. (2011) Bismark: a flexible aligner and methylation caller for Bisulfite-Seq applications. *Bioinformatics*, **27**, 1571–1572.
35. Robinson,J.T., Thorvaldsdottir,H., Winckler,W., Guttman,M., Lander,E.S., Getz,G. and Mesirov,J.P. (2011) Integrative genomics viewer. *Nat. Biotechnol.*, **29**, 24–26.
36. Yamagishi,M., Hori,M., Fujikawa,D., Ohsugi,T., Honma,D., Adachi,N., Katano,H., Hishima,T., Kobayashi,S., Nakano,K. *et al.* (2019) Targeting excessive EZH1 and EZH2 activities for abnormal histone methylation and transcription network in malignant lymphomas. *Cell Rep.*, **29**, 2321–2337.
37. Shimi,T., Kittisopikul,M., Tran,J., Goldman,A.E., Adam,S.A., Zheng,Y., Jaqaman,K. and Goldman,R.D. (2015) Structural organization of nuclear lamins A, C, B1, and B2 revealed by superresolution microscopy. *Mol. Biol. Cell*, **26**, 4075–4086.
38. Shimi,T., Pfleghaar,K., Kojima,S., Pack,C.G., Solovei,I., Goldman,A.E., Adam,S.A., Shumaker,D.K., Kinjo,M., Cremer,T. *et al.* (2008) The A- and B-type nuclear lamin networks: microdomains involved in chromatin organization and transcription. *Genes Dev.*, **22**, 3409–3421.
39. Zheng,X., Hu,J., Yue,S., Kristiani,L., Kim,M., Sauria,M., Taylor,J., Kim,Y. and Zheng,Y. (2018) Lamins organize the global three-dimensional genome from the nuclear periphery. *Mol. Cell*, **71**, 802–815.
40. Nothjunge,S., Nuhrenberg,T.G., Gruning,B.A., Doppler,S.A., Preissl,S., Schwaderer,M., Rommel,C., Krane,M., Hein,L. and Gilsbach,R. (2017) DNA methylation signatures follow preformed chromatin compartments in cardiac myocytes. *Nat. Commun.*, **8**, 1667.
41. Cooper,S., Dienstbier,M., Hassan,R., Schermelleh,L., Sharif,J., Blackledge,N.P., De Marco,V., Elderkin,S., Koseki,H., Klose,R. *et al.* (2014) Targeting polycomb to pericentric heterochromatin in

embryonic stem cells reveals a role for H2AK119u1 in PRC2 recruitment. *Cell Rep.*, **7**, 1456–1470.
42. Tardat,M., Albert,M., Kunzmann,R., Liu,Z., Kaustov,L., Thierry,R., Duan,S., Brykczynska,U., Arrowsmith,C.H. and Peters,A.H. (2015) Cbx2 targets PRC1 to constitutive heterochromatin in mouse zygotes in a parent-of-origin-dependent manner. *Mol. Cell*, **58**, 157–171.
43. Basenko,E.Y., Sasaki,T., Ji,L., Prybol,C.J., Burckhardt,R.M., Schmitz,R.J. and Lewis,Z.A. (2015) Genome-wide redistribution of H3K27me3 is linked to genotoxic stress and defective growth. *Proc. Natl. Acad. Sci. U.S.A.*, **112**, E6339–E6348.
44. Saksouk,N., Barth,T.K., Ziegler-Birling,C., Olova,N., Nowak,A., Rey,E., Mateos-Langerak,J., Urbach,S., Reik,W., Torres-Padilla,M.E. *et al.* (2014) Redundant mechanisms to form silent chromatin at pericentromeric regions rely on BEND3 and DNA methylation. *Mol. Cell*, **56**, 580–594.
45. Liu,S., Brind'Amour,J., Karimi,M.M., Shirane,K., Bogutz,A., Lefebvre,L., Sasaki,H., Shinkai,Y. and Lorincz,M.C. (2014) Setdb1 is required for germline development and silencing of H3K9me3-marked endogenous retroviruses in primordial germ cells. *Genes Dev.*, **28**, 2041–2055.
46. Huang,T.C., Wang,Y.F., Vazquez-Ferrer,E., Theofel,I., Requena,C.E., Hanna,C.W., Kelsey,G. and Hajkova,P. (2021) Sex-specific chromatin remodelling safeguards transcription in germ cells. *Nature*, **600**, 737–742.
47. Zhang,X., Liu,X., Du,Z., Wei,L., Fang,H., Dong,Q., Niu,J., Li,Y., Gao,J., Zhang,M.Q. *et al.* (2021) The loss of heterochromatin is associated with multiscale three-dimensional genome reorganization and aberrant transcription during cellular senescence. *Genome Res.*, **31**, 1121–1135.
48. Xu,Q., Xiang,Y., Wang,Q., Wang,L., Brind'Amour,J., Bogutz,A.B., Zhang,Y., Zhang,B., Yu,G., Xia,W. *et al.* (2019) SETD2 regulates the maternal epigenome, genomic imprinting and embryonic development. *Nat. Genet.*, **51**, 844–856.
49. Siegenfeld,A.P., Roseman,S.A., Roh,H., Lue,N.Z., Wagen,C.C., Zhou,E., Johnstone,S.E., Aryee,M.J. and Liau,B.B. (2022) Polycomb-lamina antagonism partitions heterochromatin at the nuclear periphery. *Nat. Commun.*, **13**, 4199.
50. Fischle,W., Wang,Y., Jacobs,S.A., Kim,Y., Allis,C.D. and Khorasanizadeh,S. (2003) Molecular basis for the discrimination of repressive methyl-lysine marks in histone H3 by Polycomb and HP1 chromodomains. *Genes Dev.*, **17**, 1870–1881.
51. Min,J., Zhang,Y. and Xu,R.M. (2003) Structural basis for specific binding of polycomb chromodomain to histone H3 methylated at lys 27. *Genes Dev.*, **17**, 1823–1828.
52. Cao,R., Wang,L., Wang,H., Xia,L., Erdjument-Bromage,H., Tempst,P., Jones,R.S. and Zhang,Y. (2002) Role of histone H3 lysine 27 methylation in polycomb-group silencing. *Science*, **298**, 1039–1043.
53. Eskeland,R., Leeb,M., Grimes,G.R., Kress,C., Boyle,S., Sproul,D., Gilbert,N., Fan,Y., Skoultchi,A.I., Wutz,A. *et al.* (2010) Ring1B compacts chromatin structure and represses gene expression independent of histone ubiquitination. *Mol. Cell*, **38**, 452–464.
54. Wang,H., Wang,L., Erdjument-Bromage,H., Vidal,M., Tempst,P., Jones,R.S. and Zhang,Y. (2004) Role of histone H2A ubiquitination in polycomb silencing. *Nature*, **431**, 873–878.
55. Grau,D.J., Chapman,B.A., Garlick,J.D., Borowsky,M., Francis,N.J. and Kingston,R.E. (2011) Compaction of chromatin by diverse Polycomb group proteins requires localized regions of high charge. *Genes Dev.*, **25**, 2210–2221.
56. Schoenfelder,S., Sugar,R., Dimond,A., Javierre,B.M., Armstrong,H., Mifsud,B., Dimitrova,E., Matheson,L., Tavares-Cadete,F., Furlan-Magaril,M. *et al.* (2015) Polycomb repressive complex PRC1 spatially constrains the mouse embryonic stem cell genome. *Nat. Genet.*, **47**, 1179–1186.
57. Gdula,M.R., Nesterova,T.B., Pintacuda,G., Godwin,J., Zhan,Y., Ozadam,H., McClellan,M., Moralli,D., Krueger,F., Green,C.M. *et al.* (2019) The non-canonical SMC protein SmcHD1 antagonises TAD formation and compartmentalisation on the inactive X chromosome. *Nat. Commun.*, **10**, 30.
58. Jansz,N., Keniry,A., Trussart,M., Bildsoe,H., Beck,T., Tonks,I.D., Mould,A.W., Hickey,P., Breslin,K., Iminitoff,M. *et al.* (2018) Smchd1 regulates long-range chromatin interactions on the inactive X chromosome and at hox clusters. *Nat. Struct. Mol. Biol.*, **25**, 766–777.
59. Wang,C.Y., Jegu,T., Chu,H.P., Oh,H.J. and Lee,J.T. (2018) SMCHD1 Merges chromosome compartments and assists formation of super-structures on the inactive X. *Cell*, **174**, 406–421.
60. Nozawa,R.S., Nagao,K., Igami,K.T., Shibata,S., Shirai,N., Nozaki,N., Sado,T., Kimura,H. and Obuse,C. (2013) Human inactive X chromosome is compacted through a PRC2-independent SMCHD1-HBiX1 pathway. *Nat. Struct. Mol. Biol.*, **20**, 566–573.
61. Quinodoz,S.A., Jachowicz,J.W., Bhat,P., Ollikainen,N., Banerjee,A.K., Goronzy,I.N., Blanco,M.R., Chovanec,P., Chow,A., Markaki,Y *et al.* (2021) RNA promotes the formation of spatial compartments in the nucleus. *Cell*, **184**, 5775–5790 .
62. Lu,J.Y., Chang,L., Li,T., Wang,T., Yin,Y., Zhan,G., Han,X., Zhang,K., Tao,Y., Percharde,M. *et al.* (2021) Homotypic clustering of L1 and B1/alu repeats compartmentalizes the 3D genome. *Cell Res.*, **31**, 613–630.
63. Sungalee,S., Liu,Y., Lambuta,R.A., Katanayeva,N., Donaldson Collier,M., Tavernari,D., Roulland,S., Ciriello,G. and Oricchio,E. (2021) Histone acetylation dynamics modulates chromatin conformation and allele-specific interactions at oncogenic loci. *Nat. Genet.*, **53**, 650–662.
64. Ulianov,S.V., Doronin,S.A., Khrameeva,E.E., Kos,P.I., Luzhin,A.V., Starikov,S.S., Galitsyna,A.A., Nenasheva,V.V., Ilyin,A.A., Flyamer,I.M. *et al.* (2019) Nuclear lamina integrity is required for proper spatial organization of chromatin in Drosophila. *Nat. Commun.*, **10**, 1176.
65. Foti,R., Gnan,S., Cornacchia,D., Dileep,V., Bulut-Karslioglu,A., Diehl,S., Buness,A., Klein,F.A., Huber,W., Johnstone,E. *et al.* (2016) Nuclear architecture organized by Rif1 underpins the replication-timing program. *Mol. Cell*, **61**, 260–273.
66. Meuleman,W., Peric-Hupkes,D., Kind,J., Beaudry,J.B., Pagie,L., Kellis,M., Reinders,M., Wessels,L. and van Steensel,B. (2013) Constitutive nuclear lamina-genome interactions are highly conserved and associated with A/T-rich sequence. *Genome Res.*, **23**, 270–280.